CDK4/6 inhibition induces a DNA damage-independent senescence-associated secretory phenotype driven by delayed activation of NF-κB

Joanna Lan-Hing Yeung,[1,*] Justin Rendleman,[1,*] Lauren Anderson,[1] Matthew Pressler,[1] Nicole Pagane,[1] Irene Duba,[1] Ria Hosuru,[1] Bat-Ider Tumenbayar,[1] Andrew Koff,[2] Viviana I. Risca[1]

[1]Laboratory of Genome Architecture and Dynamics, The Rockefeller University, New York, NY 10065, USA.
[2]Molecular Biology Program, Memorial Sloan Kettering Cancer Center, New York, NY 10065, USA.
*These authors contributed equally
Correspondence: vrisca@rockefeller.edu

Running title: CDK4/6 inhibition induces NF-κB-driven SASP in cancer

COMPETING INTERESTS

A. K. reports grants from NIH, NCI, Jennifer Linn Fund Cycle for Survival, The Maloris Foundation, and Sarcoma Foundation of America and other support from Eli Lilly during the conduct of the study as well as personal fees from Eli Lilly, Concarlo Therapeutics, and PTT Global Chemical; grants from Eli Lilly and Novartis; and other support from Atropos Therapeutics outside the submitted work. In addition, A. K. has a patent for US9889135 issued. V. I. R. has submitted a patent application (PCT/US2024/059554) for a chromatin conformation capture method.

ABSTRACT

Cellular senescence protects against aberrant cancer proliferation by enforcing stable cell cycle arrest. The best-studied triggers of senescence involve DNA damage signaling, while DNA damage-independent senescence is less understood. In the cancer context, senescence has recently been shown to be induced by CDK4/6 inhibitors (CDK4/6i), a class of targeted therapies currently applied to breast cancer and sarcoma, among other tumors. The senescence-associated secretory phenotype (SASP) can exert either pro- or anti-tumorigenic effects depending on its composition, making it a critical determinant of therapy outcome. The dependence of the SASP on the senescence trigger has been a controversial question, which we investigate here, particularly the involvement of NF-κB signaling. Using a multi-omics approach, we profiled the temporal dynamics of transcriptional and epigenetic state rewiring during therapy-induced senescence in CDK4/6i-treated liposarcoma cells over 28 days; we compared this to the effects of the DNA damaging chemotherapeutic, doxorubicin. Doxorubicin triggers an early and robust activation of p53 and NF-κB, as expected. Surprisingly, a delayed NF-κB-driven SASP signature also emerges in CDK4/6i-induced senescence after a 10-day exposure, in the absence of additional DNA damage. We replicated this effect in breast cancer cells over similar time courses. Inhibition of NF-κB blunts pro-inflammatory SASP expression without reversing cell cycle arrest in both treatment contexts, showing that NF-κB is a conserved SASP regulator, regardless of trigger and cancer type. Instead, the nature of the trigger regulates differential dynamics of the NF-κB response and additional SASP gene signatures, including a CDK4/6i-specific gene module driven by TEAD factors. Overall, our 28-day multi-omics time course reveals previously unknown dynamics of the SASP and demonstrates that both common and trigger-specific components of therapy-induced SASP can be separately tuned and uncoupled from cell cycle arrest, with implications for the rational design of adjuvant therapies.

INTRODUCTION

Cellular senescence protects against aberrant proliferation through the enforcement of stable cell cycle arrest in response to aging, oncogene activation, and other stressors [1]. Although senescence has historically been linked to activation of DNA damage[2, 3], it is now understood that cells can also undergo geroconversion—the transition from reversible to stable cell cycle arrest[4]—without incurring DNA damage[5, 6]. Unlike traditional chemotherapeutics, CDK4/6 inhibitors (CDK4/6i) are a class of targeted cancer therapies that halt cell cycle progression at the G1/S transition and induce senescence through a mechanism that does not appear to involve DNA damage[7, 8, 9, 10]. Whether senescence triggered by distinct mechanisms converges on a common cell state, or engages fundamentally different regulatory programs, continues to be debated. This remains challenging to resolve, in part because no universal biomarker defines the

senescent state[5, 11, 12]. While features such as increased lysosomal content and the formation of senescence-associated heterochromatic foci (SAHFs) are common hallmarks used to identify senescent cells[12, 13, 14], it is still unclear whether the presence or absence of DNA damage drives fundamentally distinct senescent states.

A key regulatory feature of senescence in cancer cells is the secretion of pro-inflammatory molecules, collectively known as the senescence-associated secretory phenotype (SASP)[13, 15, 16, 17]. Although NF-κB is a known master transcriptional regulator of the SASP in DNA damage-induced senescence[18, 19], its activation in CDK4/6i induced senescence remains highly debated[8, 20, 21, 22]. While this can be attributed to differences in dosages and model systems used, studies on CDK4/6i thus far remain focused on its acute effects, not the late-stage senescence response. A recent study extended the duration of CDK4/6i treatment to investigate the transition to stable arrest, identifying the angiogenic factor, ANGPTL4 as a key regulator of this process in the liposarcoma context[9]. However, the full breadth of transcriptional networks that regulate the late-stage senescence response beyond this transition remain to be investigated.

The context-dependent effects of the SASP have important implications in the benefits of therapy-induced senescence[16, 17]. The SASP's composition can vary depending on the trigger, cell type, and treatment duration, and this heterogeneity influences its pro- or anti-tumorigenic effects on the tumor microenvironment through modulation of immune responses, inflammation, cellular plasticity, and epigenome remodeling[17, 23]. Hence, an area of active interest has been to manipulate the SASP composition to achieve therapeutically beneficial outcomes through selective inhibition of its gene modules[5, 11, 17]. Given the ongoing evaluation of CDK4/6i in for cancers such as breast cancer, liposarcoma, non-small cell lung carcinoma, glioblastoma and colorectal cancer[24, 25, 26, 27, 28], we investigated this as a model of cancer therapy-induced senescence to interrogate the epigenomic regulation of the SASP.

In this study, we addressed two key unresolved questions in the senescence field: (1) How does the epigenome evolve as arrested cells progress into late-stage therapy-induced senescence, and does this differ from DNA damage induced senescence? (2) Does NF-κB play a role in driving the SASP when triggered by non-DNA damage mechanisms? We hypothesized that senescence caused by different triggers would exhibit distinct regulatory features, as blockage of CDK4/6 signaling at the G1/S boundary should give rise to a distinct cell state when compared to arrest caused by DNA damage (Fig. 1A), which can occur in either G1, S, or G2 and lead to the activation of p53[3, 29]. Moreover, since CDK4/6i's main mechanism of action does not engage in DNA damage signaling, we hypothesized that NF-κB would not be involved in shaping the resulting SASP, consistent with prior studies that did not detect NF-κB activation in CDK4/6i-induced senescence [21, 22].

We chose to address these questions in a liposarcoma model, a type of malignant mesenchymal tumor characterized by the co-amplification of *CDK4* and *MDM2* on the chromosome segment 12q13-15 in >90% of cases[30]. Traditionally, treatment is focused on surgical resection, but recurrence rates are high for patients with dedifferentiated histology and when tumor resides in the retroperitoneum[31, 32]. In these cases, the disease is managed nonoperatively, however, radiation and chemotherapy exhibit minimal efficacy for local disease[26, 30]. As such, the 10-year survival rate for these patients is only 40.1%[33]. Over the past decade, the development of CDK4/6i has emerged as a promising therapeutic strategy for patients with this challenging malignancy, as a targeted means of counteracting the CDK4 amplification[9, 25, 34]. We systematically compared the remodeling of both the transcriptome and chromatin accessibility over time in response to the CDK4/6i, palbociclib, and the DNA-damaging chemotherapeutic, doxorubicin, in a patient-derived dedifferentiated liposarcoma cell line (Fig. 1A). Importantly, these analyses were conducted with the goal of capturing not only the initial geroconversion entry phase, but also the cell state that arises in late-stage senescence, specifically up to 28 days of CDK4/6i exposure.

Our results unexpectedly show that NF-κB is activated in DNA damage-independent CDK4/6i-induced senescence, but it is not evident until cells transition beyond quiescence into stable arrest. Although there are immediate differences upon cell cycle exit which are maintained throughout all stages of senescence, we observe a core SASP module driven by NF-κB signaling that is conserved across senescence triggers, as well as a trigger-specific module for which TEAD factors are key regulators. Through pharmacological inhibition experiments, we show that targeting NF-κB and TEAD transcriptional networks can alter SASP profiles, without reversing cell cycle arrest, highlighting that SASP regulation consists of potentially separable and tunable modules apart from the impact on proliferative capacity.

RESULTS

CDK4/6i and doxorubicin both induce senescence features with distinct DNA damage levels

To determine whether cellular hallmarks of senescence were similar in response to CDK4/6i and doxorubicin, we profiled a variety of senescence assays over a 28-day time course of the CDK4/6i, palbociclib (we will refer to this treatment course as Palbo), and a 21-day time course of doxorubicin (referred to as Doxo) (Fig. 1B); we used a slightly shorter period for the Doxo experiment as doxorubicin-induced geroconversion occurs more rapidly. We observed an increasing number of cells with heightened lysosomal activity after treatment with either palbociclib or doxorubicin, as measured by positive staining for senescence-associated beta galactosidase activity (SABgal+) (Fig.

1C). In clonogenic outgrowth assays, it was apparent that less time was needed for doxorubicin to cause a drastic reduction in the number of cells capable of forming colonies after drug wash-out, indicating doxorubicin induces stable cell cycle arrest earlier than palbociclib (Fig. 1D). We also observed senescence-related chromatin changes by immunofluorescence with both treatments, consisting of increased ATRX foci and senescence-associated heterochromatin foci (SAHF) marked by macroH2A (Fig. 1E).[35, 36] Due to differences in the mechanisms of action for each drug (Fig. 1A),[7, 37, 38, 39] we anticipated the amount of DNA damage would be a distinctive feature between treatments. Indeed, DNA damage in cells following palbociclib treatment was comparable to basal levels observed in untreated cells at all timepoints, whereas the number of γH2AX DNA damage foci and 53BP1 DNA repair foci increased rapidly upon doxorubicin treatment and remained high over 21 days (Fig. 1F). Thus, our results demonstrated that CDK4/6i treatment can induce senescence without the need for excess DNA damage beyond what was detected in untreated cycling cells.

Global changes in the chromatin and transcriptional landscape define drug-induced senescence trajectories

We next wanted to compare how transcriptional regulation changes over time between these two distinct modes of therapy-induced senescence. To that end, we performed RNA-seq and ATAC-seq in liposarcoma cells treated with palbociclib or doxorubicin and sampled over early and late geroconversion, capturing the same timepoints as before (Fig. 1B). We analyzed these two data types and mapped drug responses to determine how the global transcriptome changed over time, relative to changes in peak accessibility, after assessing for standard data quality metrics (Supplementary Table 1). In both RNA-seq & ATAC-seq, sample distance measures and principal component analysis showed that, as expected, samples grouped by drug treatment, which were both distinct from untreated controls (Cycling) (Fig. 2A, B). Global analyses of both transcriptome (RNA-seq) and DNA accessibility landscape (ATAC-seq) dynamics showed subclusters representing early-, mid-, and late-phases of senescence driven by each drug (Fig. 2A). The first two principal components (PCs), accounting for ~60-70% of variation, were able to largely separate samples by drug and timepoint (Fig. 2B). These overall changes corresponded to the timing of progressive geroconversion as observed by SABgal+ cells, SAHF formation, and reduced clonogenic outgrowth (Fig. 1).

We asked how differing levels of DNA damage influences molecular changes between these distinct types of therapy-induced senescence and identified 3,744 differentially expressed genes across drug treatments and time points in our RNA-seq data (Fig. 2C; Supplementary Table 2). Genes could be grouped into four expression-based clusters that distinguish the effects of each drug, which was further broken down depending on the dynamics of response. Assessing global patterns, we noticed that most

downregulated genes were common across the two treatments, annotated as “Shared-down,” and this cluster was enriched for genes involved in cell cycle progression. On the other hand, SASP genes were largely split across clusters that were upregulated, either by both drugs (“Shared-up”), or preferentially by one drug (“Palbo-upregulated” and “Doxo-upregulated”) (Fig. 2C). Taken together this suggests that, while stable arrest is a common feature between these two forms of therapy-induced senescence, their transcriptomic compositions have distinct outputs. We also noted that while most differentially regulated genes were of a protein coding nature, approximately 20% were annotated as lncRNA (Supplementary Fig. 1A).

Next, we performed differential peak analysis on our ATAC-seq data, comparing genome-wide chromatin accessibility at each timepoint relative to Cycling and day 3-treated samples, within each drug time course (summarized in Supplementary Fig. 1B). Out of the 215,671 unique ATAC-seq signal peaks in our non-redundant master peak set, 88,735 peaks (41%) underwent significant changes: a total of 49,107 unique peaks increased in accessibility in at least one drug, while 42,164 unique peaks decreased (Fig. 2D, E). We asked whether accessibility changes due to drug treatment were largely specific or shared, and we found that while palbociclib and doxorubicin did have unique sets of peaks changing in either direction, reflecting drug-distinct responses, they also have common regions with altered accessibility, denoting a shared chromatin component of therapy-induced senescence (Fig. 2D, E). Of note, while most ATAC-seq peaks with increasing accessibility were localized to enhancer-like regions (i.e., distal intergenic or intronic), those with decreasing accessibility had a stronger preference for promoter proximal regions (Supplementary Fig. 1C, D). We observed that the contrast between accessibility at transcription start sites (TSS) and surrounding regions dropped toward later stages of senescence; however, our libraries maintained a TSS-to-background accessibility ratio that passed our data quality standards (Supplementary Fig. 1E). Interestingly, we also observed that nucleosome peaks in late-stage geroconversion were left-shifted, consistent with a reduction in inter-nucleosome linker lengths (Supplementary Fig. 1F). Given previous work, we expected largescale chromatin reorganization and potential decompaction upon geroconversion[40, 41, 42]; we found that globally, doxorubicin induced a comparable number of ATAC-seq peaks with increasing and decreasing accessibility, while palbociclib treatment resulted in more peaks with increased accessibility overall (Fig. 1G, H).

The shutdown of E2F target genes is more efficient with direct CDK4/6 inhibition

Given the nature of stable growth arrest in therapy-induced senescence, and the targeted effects of CDK4/6i on Rb (Fig. 1A), we asked whether E2F transcriptional targets were being shut down similarly between palbociclib and doxorubicin treatments. Indeed, E2F targets were enriched amongst “Shared-down” genes (Supplementary Fig.

2A B; Supplementary Table 3) corresponding to cell cycle exit. Although both drugs led to an eventual attenuation of E2F target genes (Supplementary Fig. 2C, D), this was achieved at the earliest timepoints with palbociclib while it was a gradual shutdown with doxorubicin (RNA Cluster 1 in Fig. 2C; Supplementary Fig. 2E), underscoring the direct inhibitory effect on G1/S blockade imposed by CDK4/6i. We noticed the smaller subcluster of genes decreased expression (RNA Cluster 2; Fig. 2C) behaved very differently, by shutting down earlier in the Doxo time course than in Palbo. This cluster was not enriched for cell cycle progression or E2F targets (Supplementary Fig. 2A, B), but instead contained several genes related to cell adhesion and laminin interactions (e.g., *NID1*, *ITGB4*, *COL4A2*). As for the downregulation of cell cycle progression genes, the E2F shutdown was also observed at the chromatin level in our ATAC-seq data, with E2F motif-containing peaks decreasing in accessibility in response to both palbociclib and doxorubicin (Supplementary Fig. 2F, G). Although there was a shared set of downregulated E2F motif-containing loci, there was also many drug-specific E2F sequences that became less accessible (Supplementary Fig. 2F), suggesting that while both drugs converge on inhibiting the same set of E2F target genes, they may do so through distinct changes to the E2F binding landscape.

Signatures of enriched transcriptional regulators in therapy-induced senescence

We next focused our attention on characterizing features of upregulated peaks and genes, as these would likely include drivers of geroconversion and not solely reflect cell cycle exit. To understand what transcription factors may be binding in regions of newly open chromatin, we determined enriched motifs under increasingly accessible peaks at each timepoint in the Palbo and Doxo experiments (Supplementary Fig. 3A; Supplementary Table 4). Since static ATAC-seq peaks often contain many of the same motifs found in dynamic peaks, due to their roles in cell identity and maintenance, we focused on identifying motifs with the greatest dynamic contrast. To this end, we performed motif enrichment analysis comparing regions with increasing accessibility against regions with decreasing accessibility at each timepoint (see Methods). In line with what others have reported previously in senescence,[43, 44] the AP-1 family of transcription factors was strongly enriched in response to DNA damage and increased in enrichment over time with CDK4/6 inhibition (Supplementary Fig. 3A). Additional motifs with similar patterns of increased accessibility were from the CEBP, STAT, TEAD, GATA, SOX and FOX families of transcription factors, which play roles in cell fate determination, metabolism, and inflammatory responses.[45, 46, 47, 48, 49, 50, 51, 52, 53, 54, 55] We asked whether these transcription factor effects could also be observed in our RNA-seq data, and to test this we looked at activation scores of upstream transcriptional regulators predicted by Ingenuity Pathway Analysis (IPA) (Supplementary Fig. 3B; Supplementary Table 5). In these networks, we found *JUN*, a member of the AP-1 family, was among the top predicted transcriptional regulators across four out of five

upregulated RNA clusters, consistent with a role in general chromatin remodeling. On the other hand, we found *STAT3* and *CEBPB* displayed stronger activation scores among Palbo-upregulated genes, whereas *TP53* had the highest score for the Doxo cluster with early induction after treatment. Additionally, *NFKB1* (encoding a subunit of NF-κB) appeared in the network that was predicted to control shared upregulated genes, as well as clusters specific to each drug (Fig. 3B), which also aligned with ATAC-based motif enrichment results (Fig. 3A).

p53 activity in senescence is dependent on DNA damage

Performing pathway enrichment and Gene Set Enrichment Analysis (GSEA) on our RNA-seq data, we found the p53 pathway overrepresented among genes that were specifically induced by doxorubicin treatment (Fig. 3A; Supplementary FIg.S4A; Supplementary Table 3). Examining genes under the "P53 PATHWAY" term that met our significance criteria (fold change > 4 and *Padj* < 0.05), confirmed many were more strongly upregulated in Doxo samples compared to Palbo (Fig. 3B). This preferential doxorubicin-induced upregulation was also observed for well-established p53 targets, such as p21 (*CDKN1A*) and *MDM2* (Fig. 3C). Moreover, the number of p53 targets in Doxo-upregulated clusters was much higher than in Palbo-upregulated clusters (Fig. 3D, E).

To further compare the effects of each condition on p53 target expression, we overlapped our list of significantly changing genes with previously reported p53 targets curated by Fischer,[56] as well as genes associated with the "P53 PATHWAY" Hallmark term (Fig. 3F). Overall, doxorubicin treatment resulted in a stronger induction of target expression compared to palbociclib treatment (Fig. 3F). Taken together, doxorubicin clearly displayed a stronger activation of p53 signaling, however, a subset of p53 targets also increased in response to palbociclib; we found that many of these genes were also annotated as SASP or NF-κB targets, suggesting their upregulation in palbociclib-treated cells may not be exclusively or primarily regulated by p53 (Fig. 3E).

To investigate whether a differential p53 chromatin binding signature existed between palbociclib- and doxorubicin-induced cell cycle arrest, we analyzed Tn5 insertion site coverage within 1-kb of p53 motifs located in ATAC-seq peaks with increased accessibility. Among Doxo-upregulated ATAC-seq peaks, both the total number of peaks containing p53 motifs as well as the accessibility centered on the motif was higher than in Palbo (Fig. 3G). This trend was also observed in shared upregulated peaks, though the difference was less pronounced; in contrast, in Palbo-upregulated peaks, accessibility was not preferentially concentrated at p53 motifs (Fig. 3G). These findings suggest that doxorubicin-induced cell cycle arrest is associated with a stronger p53 signature at both the gene expression and chromatin accessibility levels.

Differential regulatory pathways distinguish doxorubicin- and palbociclib-driven therapy-induced senescence

We next focused on drug-specific responses, based on our finding of Hallmark gene sets and Reactome pathways with strong preferential enrichment scores for Palbo (Supplementary Fig. 4B) or Doxo (Supplementary Fig. 4C) in the GSEA results. From the drug-specific clusters in our RNA-seq results (Fig. 2C), we used log2FC values to better visualize the distinct differences between these subclusters (Fig. 4A; Supplementary Table 2). We again performed an IPA upstream analysis, only this time directly looking for the most differential predicted regulators between drugs (Fig. 4B; Supplementary Table 5). Approaching the data in this way reiterated a p53-centered network specific to doxorubicin, but it also revealed a palbociclib-specific network involving HIF-1 and TGFβ regulation (Fig. 4A, B). Genes in this cluster included many related to the extracellular matrix (ECM) (Supplementary Fig. 4A), including *COL3A1, COL5A2, SERPINE1*, and *TIMP3*; notably these were also classified as SASP factors under our criteria, suggesting this may represent a CDK4/6i-specific SASP signature.

Given these distinct transcriptional programs, we next sought to identify differentially enriched motifs between drugs at increased accessibility regions that could be involved in drug-distinct gene expression changes. To do so, we performed motif enrichment analysis on upregulated ATAC-seq peaks that were significantly different between drugs (Fig. 4C; Supplementary Table 6). This analysis identified several Palbo-enriched motifs, including CEBPβ, TEAD4, MEF2A/B/C, SOX5 and GATA3 (Fig. 4C, left)—transcription factors that can modulate binding to mesenchymal enhancer elements and are involved in the epithelial-mesenchymal transition process,[57, 58, 59, 60, 61, 62, 63, 64] which was also reflected in our RNA-seq data (Supplementary Fig. 4A, B).

Consistent with our broader motif enrichment results (Supplementary Fig. 3A), this targeted differential analysis found the AP-1 family enriched in regions with increased accessibility specific to doxorubicin treatment (Fig. 4C, right), reinforcing AP-1's preferential role in a DNA damage-induced senescence transcriptional response. We also observed preferential enrichment of ZIC1 in Doxo-upregulated accessible regions, a factor overexpressed in liposarcomas and implicated in tumor invasiveness.[65] Taken together, these findings describe a chromatin landscape where, although many of the same transcriptional motifs were enriched across regions of increased accessibility shared between the responses to both drugs (Supplementary Fig. 3A), when we specifically look at regions that became more accessible in one condition (Fig. 4C), these regions contained binding sites for alternative transcription factors that may activate distinct modules of the senescence program and differentiate RNA outputs (Fig. 4A, B).

A shared senescence transcriptomic signature is driven by NF-κB signaling across cancer cell types

Although multiple features of therapy-induced senescence varied between doxorubicin and palbociclib treatments (e.g., DNA damage activation, p53 signaling, and a large fraction of RNA and chromatin accessibility changes), we were particularly interested in what aspects these two very different drivers of geroconversion had in common, with respect to regulatory networks and transcriptional outputs. To investigate this, we focused on shared upregulated genes (RNA Cluster 7 in Fig. 2C), which were enriched in inflammation-associated pathways (Fig. 5A). We previously noted NF-κB appeared as a mutual signature of therapy-induced senescence in both drugs (Supplementary Fig. 3A, B). Given the nature of NF-κB as a pivotal mediator of inflammatory responses,[66] we asked whether the shared transcriptional response may be NF-κB-driven. Indeed, when we looked at predicted upstream regulators of genes comprising the shared RNA response, the NF-κB complex and RELA, the p65 subunit of NF-κB, emerged as the top candidates (Fig. 5B). GSEA further supported this, showing the Hallmark pathway "TNFA SIGNALING VIA NFKB" was similarly enriched at day 14 of both treatments, relative to untreated cycling controls and day 3 within each drug time course, representing early response (Fig. 5C). Furthermore, we identified 40 NF-κB target genes within the shared cluster, half of which were annotated as SASP genes (Fig. 5D), and analyzed their RNA levels at days 3 and 14 of treatment (Fig. 5E). Both drugs showed a significant increase in expression over time, consistent with a progressive NF-κB response. However, this response was delayed in palbociclib-treated cells, with the median fold change at day 14 resembling that of doxorubicin at day 3.To assess whether delayed NF-κB activation also occurs in other cancer types treated with CDK4/6i, we performed RNA-seq on MCF7 breast cancer cells treated with 100 nM palbociclib and 10 nM fulvestrant—the standard-of-care regimen for ER+ breast cancer. A previous study did not report NF-κB activation with 5 days of CDK4/6i treatment using the MCF7 cell line[21]. Therefore, we wondered whether later timepoints would show NF-kB activation regulating the SASP in this system as well. We confirmed that CDK4/6i induces senescence in MCF7 cells without triggering excess DNA damage beyond what is observed in cycling cells, unlike doxorubicin (Fig. 5F, G). Transcriptomic analysis revealed that the 7,510 significantly altered genes based on a *Padj* threshold of < 0.05, which are part of NF-κB-related pathways, are enriched in cluster 3; a group of genes that are modestly upregulated at early time points (days 3-5) but show strong induction after day 10 (Fig. 5H, I). Thus, even in a model where NF-κB activity was previously undetected in short-term studies,[21, 22] we observed the eventual activation of NF-κB as a late treatment response. This supports the notion that NF-κB-SASP network activation is a shared feature of therapy-induced senescence across cancer types (Fig. 5; Supplementary Fig. 5).

Notably, while both drugs shared a core set of upregulated NF-κB target genes, additional drug-specific NF-κB target genes, many of which are additional SASP factors, were identified within drug-distinct RNA clusters (Supplementary Fig. 5B). However, when we compiled a list of SASP genes that were induced in our context by either drug, performing an upstream analysis with IPA predicted the Palbo-specific SASP was driven by AGT and TGFβ, the Doxo-specific SASP was driven by IFN-γ and p53, while only the shared SASP was likely driven by TNF and NF-κB (Supplementary Fig. 5C).

Increased chromatin accessibility at putative NF-κB binding sites occurs in both types of therapy-induced senescence

Observing both drugs give rise to distinct effects on the chromatin landscape (Fig. 2D; Supplementary Fig. 1G), we asked whether the shared and drug-specific NF-κB target gene expression patterns could be explained by a model where there is a common activation of NF-κB, however differential effects on transcription are determined by motif accessibility. Therefore, we next investigated how the NF-κB signature was reflected in chromatin accessibility changes between the two treatments. Motif enrichment analysis of shared peaks with increased accessibility revealed significant enrichment of NF-κB family motifs in both drugs (Fig. 6A). We found that among all ATAC-seq peaks that displayed increasing accessibility in either condition (N = 49,107), there were 9,112 regions containing at least one NF-κB motif, however, in line with our model, only 1,718 of these were in mutual regions of increasing accessibility between drugs, while a majority of NF-κB motif-containing ATAC-seq peaks with increasing accessibility were instead drug-specific (Fig. 6B).

To determine whether changes in accessibility at putative NF-κB binding sites contribute to the shared upregulation of NF-κB target genes, we looked specifically at regions within 50 kb of these genes (see Methods). Tn5 insertion site coverage around the NFKB1 motif in these nearby ATAC-seq peaks showed increased accessibility in both treatments relative to cycling or day 3 controls (Fig. 6C). Specifically, we observed shared increases in accessibility within the gene bodies of NF-κB target genes and particularly around their transcription termination sites, including *IL1A, IL1B, CXCL1, and CXCL8* (Fig. 6D), which are also part of the shared SASP. This is consistent with their transcriptional upregulation in both drug treatments. Interestingly, we also detected increased accessibility in distal intergenic regions near these genes (Fig. 6D); these regions correlate with previously characterized RELA binding sites and H3K27ac-depleted regions in untreated cells (Fig. 6D), providing evidence that NF-κB may only gain access to these regulatory elements upon drug treatment.

Further motif enrichment analysis of genomic regions with increasing chromatin accessibility near transcriptionally induced genes reaffirmed the consistent enrichment

of NF-κB family motifs across both drugs (Supplementary Fig. 6A; Supplementary Table 7). Notably, these motifs were highly enriched in drug-upregulated RNA clusters but were less enriched—or absent—near shared downregulated genes (Supplementary Fig. 6B, C; Supplementary Table 7). These findings suggest that, while a proinflammatory NF-κB-driven SASP arises early in doxorubicin treatment due to excess and persistent DNA damage, it is gradually activated in palbociclib-treated cells following the establishment of stable cell cycle arrest; a generalizable response despite the distinct mechanisms through which the two drugs induce senescence.

Distinct components of the SASP, including NF-κB, can be uncoupled from stable cell cycle arrest

To verify the shared NF-κB signatures found in the multi-omics analysis, we performed immunofluorescence on p65 to directly measure NF-κB activation; phosphorylation of IkB by the IKK complex leads to proteasomal degradation and subsequently the release of the p50/p65 canonical subunits that form NF-κB.[67] This results in the rapid and transient nuclear translocation of NF-κB where it can bind to chromatin to regulate transcription of its target genes. In both treatments, we observed p65 localization to the nucleus with timing that correlated approximately with the timing of stable cell cycle arrest (Fig. 7A; Supplementary Fig. 7A), i.e., steadily increasing up to day 14 in response to palbociclib and much earlier by day 3 in doxorubicin.

After verifying that NF-κB was indeed being activated in both drugs, we attempted to alter the NF-κB-driven shared SASP response through pharmacological inhibition with BAY11-7082 (BAY)[68] during both treatments, after senescence was established (Supplementary Fig. 7B). Principal component analysis shows NF-κB inhibition had minimal impact on the overall transcriptome, as BAY- and DMSO-treated samples clustered together within each drug group (Fig. 7B). However, BAY suppressed expression of key shared NF-κB target SASP genes, *CXCL1, CXCL8, IL1A, IL1B, GMCSF (CSF2), IL6 and SOD2* (Fig. 7C; Supplementary Fig. 7C, D). Beyond these, NF-κB inhibition downregulated 57 shared genes as well as additional drug-specific targets (Supplementary Fig. 7E), suggesting that while NF-κB is a common feature of senescence, its regulated may differ across treatments. Like previous studies of NF-κB in other types of senescence[18, 69], inhibiting its activity was not enough to reverse senescence, as indicated by no differences in clonogenic outgrowth assays (Fig. 7D). Hence, although NF-κB activation does not appear to be necessary for maintaining stable arrest, it is responsible for driving part of the inflammatory SASP response.

Given the growing interest in targeting specific components of the SASP, [69, 70, 71] we asked whether additional trigger-specific branches of the SASP could be uncoupled from cell cycle arrest, in addition to the shared NF-κB-driven program. We focused on

the TEAD, a family of transcription factors involved in the HIPPO pathway, whose motifs were preferentially enriched near genes and in accessible regions upregulated by palbociclib compared to doxorubicin (Fig. 4C; Supplementary Fig. 6A). Pharmacological inhibition of TEAD with MYF-01-37[72] suppressed key palbociclib-upregulated SASP factors, most notably *ANGPTL4* and *IGFBP3*; without disrupting stable cell cycle arrest (Fig. 7E, F). These results identify TEAD as a previously unrecognized regulator of a CDK4/6i-induced SASP program and demonstrate that both shared and drug-distinct branches of the SASP can be selectively modulated.

DISCUSSION

Therapeutic response in various cancers is in part determined by how effectively tumors are driven into stable arrest. Understanding the evolution of the corresponding SASP that arises in different therapies will be essential in identifying new targeted approaches that can drive more favorable outcomes.

Here we have mapped the temporal dynamics of epigenomic and transcriptomic states that develop during therapy-induced senescence, which appear dramatically different when triggered by a DNA-damaging agent (e.g., doxorubicin) or a DNA damage-independent mechanism (e.g., the CDK4/6 inhibitor palbociclib). Unlike replicative senescence that arises during aging[73], therapy-induced senescence is an acute response to cancer treatment, exhibiting many features of canonical senescence although mediated through distinct molecular triggers[10, 71, 74]. Our findings indicate that most changes in both chromatin accessibility and the transcriptional landscape that occur during prolonged cell cycle arrest are in fact drug-distinct, however there exists a set of shared molecular responses across both drugs, which emerge at trigger-specific rates. Our results bring new insights that help explain conflicting reports on various features of therapy-induced senescence, including the involvement of NF-κB in therapeutics that do not rely on DNA damage as a mechanism of action.

Furthermore, while the field has long viewed stable arrest and the SASP as tightly linked, prior studies have challenged this assumption by showing that these two hallmarks of senescence can be uncoupled[69, 70, 71]. Our findings contribute to this growing, but still under-explored body of work. We were able to suppress both shared and CDK4/6i-distinct components of the SASP while preserving cell cycle arrest, by inhibiting NF-κB and TEAD, two key transcriptional regulators identified from our multi-omics analysis. This suggests that selective inhibition of targeted components of the SASP could modulate the long-term effects of treatment across different drug classes.

Although several studies have pointed to CDK4/6i-induced senescence occurring without DNA damage [7, 8, 9, 21], some recent reports do show DNA damage is triggered following CDK4/6i washout, amongst cells that re-enter the cell cycle[75, 76]. In our study,

we did not detect significant DNA damage following prolonged CDK4/6i treatment, even by day 28, which we consider a late-stage senescence timepoint. Our experimental design did not include washout, and we focused on stably arrested populations. The lack of persistent DNA damage supports the notion that CDK4/6i triggers senescence through distinct mechanisms from genotoxic agents like doxorubicin. This is consistent with other observations of DNA damage-independent senescence, such as that triggered by over expression of the endogenous CDK4/6 inhibitor, p16[5, 77]. This difference is reflected in their divergent transcriptomic and chromatin accessibility profiles that remain distinct over time. One of the most distinct differences between treatments was their p53 signature, for which doxorubicin elicited a much stronger response relative to CDK4/6i, in contrast with a recent study in CDK4/6i-treated fibroblasts where they reported a p53-driven SASP [22].

In addition to the significant trigger-specific transcriptional responses, we unexpectedly observed a SASP module shared by CDK4/6i- and doxorubicin-induced senescence, albeit with distinct temporal dynamics. Both treatments induce dramatic chromatin remodeling: reduced accessibility at promoters coinciding with decreased expression of E2F target genes, with increased accessibility predominantly at putative enhancer elements. NF-κB motifs stood out as being similarly enriched in both treatments, in contrast to most other motifs that showed differential levels of enrichment. Notably, we observed increased accessibility at putative NF-κB binding sites around shared upregulated SASP genes, coinciding with nuclear accumulation of NF-κB and stable arrest.

Although NF-κB's role in oncogene-induced senescence is well-established[18, 19], its activation in CDK4/6i-induced senescence was surprising, as prior studies which focused on early responses failed to detect NF-κB activity[21, 22]. This discrepancy likely reflects differences in the duration of treatment. We did not observe increased NF-κB activity in MCF7 breast cancer cells at day 5 of treatment, a similar observation to that made by Lee *et al.* [21]. However, by increasing the duration of CDK4/6i treatment (i.e., 14, 21, 28 days), we observed delayed but robust NF-κB activation across both liposarcoma and breast cancer cells. This reveals a previously underappreciated inflammatory component of CDK4/6i-induced senescence, with potential implications for long-term therapeutic outcomes.

These findings raise important questions about the temporal regulation of the SASP across different senescence triggers. A prominent example of this is increased accessibility at AP-1 motifs, which was shown to activate enhancers in response to CDK4/6i in breast cancer[43]. Here, AP-1 activation emerged as a global response, with dynamics that differed between treatments: while immediately enriched upon doxorubicin exposure, accessible AP-1 sites gradually accumulated with palbociclib,

ultimately reaching comparable enrichment levels after a month of treatment. AP-1 is known to act synergistically with NF-κB to drive the expression of its target genes[78, 79, 80]. Our results are consistent with cooperation between AP-1 and NF-κB to drive genome-wide chromatin rewiring, with both factors exhibiting delayed activation coinciding with palbociclib-induced geroconversion, offering an explanation for the timing and magnitude differences of NF-κB-driven SASP activation across treatments.

Our results underscore two important considerations, which likely contribute to apparent discrepancies in recent studies: 1) the importance of the underlying chromatin landscape that can vary intrinsically by cell type and extrinsically by trigger response, and 2) the dynamic nature of the SASP. In conclusion, we propose a model in which both doxorubicin and CDK4/6i induce senescence through distinct molecular mechanisms that converge over time, leading to NF-κB activation (Fig. 8A). This promotes a shared senescence response that manifests as a common set of cytokines and chemokines, which are secreted as part of the SASP (Fig. 8B). However, at the same time differential chromatin accessibility, possibly through differential chromatin remodeler activity (e.g., targeted by AP-1), allows NF-κB to act on alternative genomic regions to give rise to drug-specific expression and temporal patterns.

Here, we show that a subset of shared SASP factors *(CXCL1, CXCL8*, *IL6*, *IL1A*, and *IL1B*) can be effectively suppressed by NF-κB inhibition; many of these have known tumor-promoting functions, including immunosuppression, metastasis, and chemoresistance[17, 81, 82, 83, 84, 85, 86]. Beyond shared targets, CDK4/6i not only upregulates additional NF-κB-target SASP genes compared to doxorubicin, but also induces a distinct ECM-enriched SASP program regulated by TEAD, including *ANGPTL4*, a recently identified regulator of geroconversion in liposarcoma[9]. Future work is needed to understand the interplay and regulation between CDK4/6i-distinct and shared components of the SASP. Nonetheless, our data suggests a paradigm shift in the way we think about the clinical implications of CDK4/6i treatment. While it may offer initial benefits to patients over traditional chemotherapy, over time it leads to the emergence of a pro-inflammatory SASP driven by NF-κB that could promote tumor progression. The deeper understanding of transcriptional and epigenetic dynamics made possible by our extended comparative time course provides a potential solution to this problem. We showed that the expression of both NF-κB- and TEAD-driven SASP can be separately reduced by small molecule inhibition of these transcription factors, without compromising cell cycle arrest. The senescence response and SASP may therefore be tunable by adjuvant therapies to diminish pro-tumorigenic side effects.

By addressing gaps in our understanding of long-term CDK4/6i-induced senescence, these results provide insights into its molecular regulation and effects on cell fate

decisions over time. This will be useful in furthering our understanding of patient outcomes, especially as new CDK4 and CDK2 inhibitors enter the clinic.

DATA AND MATERIALS AVAILABILITY

All sequencing datasets have been deposited in the Gene Expression Omnibus (GEO) database. Code supporting analysis of sequencing datasets can be found at https://github.com/yeungj234/Manuscript_Figures.
Further information and request for resources and reagents should be directed to and will be fulfilled by the lead contact, Dr. Viviana Risca (vrisca@rockefeller.edu).
ATACseq: GSE295258 (Reviewer token: ojihqayqnhethgj)
RNA-seq: GSE295260 (Reviewer token: qbsxqqouzxufzub)
CUT&Tag: GSE295261 (Reviewer token: shapgsuwfnqthcp)

ACKNOWLEDGMENTS

J. L. Y. acknowledges support from a Natural Sciences and Engineering Research Council of Canada Postgraduate Scholarships – Doctoral scholarship. J. R. was supported by the American Cancer Society – Fairfield Research Council– Postdoctoral Fellowship, PF-23-1034949-01-CCB, https://doi.org/10.53354/ACS.PF-23-1034949-01-CCB.pc.gr.168157. L. J. A acknowledges support from the NSF Graduate Research Fellowship Program (1946429). This work was supported in part by a V Scholar Award (V2019-011) from the V Foundation for Cancer Research, by a Starr Cancer Consortium Grant (I16-0058), a Scholar Award from The Rita Allen Foundation (S-2108-02147), and a Career Scientist Award from the Irma T. Hirschl/Monique Weill-Caulier Trust.

We acknowledge support from the Rockefeller University Genomics Resource Center (RRID:SCR_020986), and the High-Performance Computing Resource Center (RRID:SCR_025889). We thank Andrew Scortea for administrative support and his work in setting up the Risca laboratory. We thank Wei Zhou for technical assistance. We acknowledge Novogene for providing RNA and DNA sequencing services. We thank all members of the Risca and Koff laboratories, Hironori Funabiki, Lydia Finley and Junyue Cao for insightful discussions and advice.

AUTHOR CONTRIBUTIONS

J. L. Y.: Conceptualization of project, performed experiments, data analysis, visualization and curation, manuscript writing and editing. J. R.: Performed experiments, data analysis, manuscript writing and editing, and provided mentorship. N. P.: Bioinformatics analysis. L. J. A.: Performed experiments, image analysis and manuscript editing. M. P.: Performed experiments and manuscript editing. I. D.: Bioinformatics analysis. R. H.: Bioinformatics analysis. B. T.: Performed experiments and image analysis. A. K.: Mentorship, resources, and manuscript editing. V. I. R.: Conceptualization of project, resources, project supervision, mentorship, funding acquisition, manuscript writing and editing.

MATERIALS AND METHODS:

Cell lines and cell culture

Human LS8817$^{TetON\ FLAG\text{-}MDM2}$ liposarcoma cell line was a gift from Dr. Andrew Koff's laboratory at Memorial Sloan Kettering Cancer Center and has been extensively characterized in the literature.[65, 87, 88, 89, 90, 91] LS8817 have previously been described using the nomenclature DDLS8817 (RRID:CVCL_M814). Cells were cultured in DMEM high glucose no glutamine (Cat# 11960044, Gibco™, Waltham, Massachusetts), supplemented with 9% Fetal Bovine Serum (Cat# 10082147, Gibco™), 1% of 100x GlutaMAX™ Supplement (Cat# 35050061, Gibco™) and 1% of 10,000U/mL Penicillin/Streptomycin (Cat# 15140122, Gibco™) and maintained at 37°C and 5% CO_2. Cells were authenticated by performing STR profiling to another LS8817 isogenic cell line.

Human MCF-7 cells (RRID:CVCL_0031) were cultured in in 75 cm2 flasks DMEM/F-12 (#Cat 10565018, Thermo Fisher Scientific, Waltham, Massachusetts) supplemented with GlutaMAX, 10% Fetal Bovine Serum (Cat# F4135, Sigma-Aldrich) and 1% Penicillin-Streptomycin at 37 °C and 5% CO2. Prior to their use, MCF7 cell identity was verified by STR profiling.

Cells were passaged at a 1:3 ratio every 3 days and regularly tested for mycoplasma.

RNA-sequencing

RNA extraction was done using the Quick-RNA Microprep Kit (Cat# R1050, Zymo Research, Irvine, California). Total RNA from at least 2 biological replicates per condition was sent to Novogene for stranded library preparation and sequencing. cDNA libraries were made with NEBNext® Ultra™ II Directional RNA Library Prep Kit for Illumina (Cat# E7765, New England Biolabs, Ipswich, Massachusetts) and sequenced on Illumina NovaSeq 6000 Sequencing System as 150-base pair-end reads.

ATAC-sequencing

ATAC libraries were generated following Corces et al. protocol for OMNI-ATAC.[92] In brief, cells were treated in culture medium with DNase (Cat# LS002007, Worthington, Lakewood, New Jersey) at a final concentration of 200 U/mL at 37 °C for 30 minutes, then washed twice with PBS at 500 RCF, room temperature (RT). Approximately ~50,000-60,000 cells were used for each transposition reaction. Following permeabilization, 2.5 µL of Illumina TDE1 enzyme (Cat# 20034198, Illumina , San Diego, California) was used for transposition at 37 °C for 30 minutes. Libraries were PCR amplified for 8-13 cycles with Illumina i5 or i7 barcoded primers and were cleaned up pre- and post-amplification following the manufacturer's instructions using Zymo DNA Clean and Concentrator-5 Kit (Cat# D4014, Zymo Research). At least 2 technical replicates and 2 biological replicates per condition were sequenced. Fragment length distribution and DNA amount was quantified via TapeStation and Qubit to assess for

quality prior to sequencing. Libraries were sequenced on the Illumina NovaSeq 6000 or on the NextSeq 1000 Sequencing System.

CUT&Tag sequencing

CUT&Tag on untreated cycling LS8817 cells was performed following the protocol from Kaya-Okur et al.[93] and was previously described in Soroczynski et al.[94] Antibodies used include: Tri-Methyl-Histone H3 (Lys27) (C36B11) Rabbit mAb (9733T, Cell Signaling Technology, Danvers, Massachusetts), 1:50; Anti-Histone H3 (acetyl K27) antibody - ChIP Grade (ab4729, Abcam, Cambridge, United Kingdom), 1:100; Guinea Pig anti-Rabbit IgG (Heavy & Light Chain) antibody (ABIN101961, Antibodies-online, Aachen, Germany), 1:100.

Drug treatments

Cells were passaged at a 1:3 ratio one day before drug treatment. For samples sent for sequencing, cells were treated with either 1 µM palbociclib (Cat# S1116, Selleck Chemicals, Houston, Texas) or 100 nM doxorubicin (Cat# S1208, Selleck Chemicals), with media changes every 2–3 days until harvest. For NF-κB inhibition experiments, 10 µM BAY11-7082 (Cat# S2913, Selleck Chemicals) was co-administered with 1 µM palbociclib in cells that had been treated with Palbo 3 days before harvest. For the corresponding timepoints in Doxo, cells were treated with 100 nM doxorubicin for 24 hours, after which the drug was washed out. 10 µM BAY11-7082 was then added for 2–3 days prior to harvesting the Doxo-treated cells. For TEAD inhibition experiments, cells were treated with 1 µM palbociclib for 3 days before co-administration with 10 µM MYF-01-37 (Cat# S8950, Selleck Chemicals) until harvest. Stock solutions were prepared as followed: palbociclib (10 mM in ultrapure dH_2O, stored at -80°C), doxorubicin (1 mM in ultrapure dH_2O, stored at -20°C), BAY11-7082 and MYF-01-37 (50 mM in DMSO, stored at -80°C).

Immunofluorescence

50,000-60,000 cells were plated on acid washed glass coverslips and allowed to adhere overnight. Cells were fixed for 15 minutes with 4% formaldehyde followed by permeabilization with 0.1% Triton-X. Blocking was done with 0.5% Tween-20 and 1% normal goat serum for 30 minutes-1 hour. Antibody dilutions are as follows: ATRX (Cat# A301-045A, Bethyl, Montgomery, Texas) 1:2000, macroH2A (Cat# sc-377452, Santa Cruz, Dallas, Texas) 1:500, γH2A.X (Cat# 05-636, Millipore, Burlington, Massachusetts) 1:1000, 53BP1 (Cat# ab172580, Abcam) 1:1000, NF-κB p65 (Cat #8242, Cell Signaling Technology) 1:800. Primary antibody incubations were done at 4°C overnight. The next day, secondary Alexa Fluor™ antibodies (Cat# A-11004 and A-11008, Invitrogen, Waltham, Massachusetts) were diluted 1:500 with 1:2000 Hoechst (Cat# H3570, Fisher Scientific, Waltham, Massachusetts) and incubated for 1 hour at RT. All reagents,

including antibodies, were diluted in 1X PBS. All steps were followed by 3 washes of 1X PBS. Coverslips were mounted on homemade mounting medium (1 mL 10X PBS, 9 mL Ultrapure glycerol and 50mg of N-propyl gallate (Cat# A10877-06, Alfa Aesar, Ward Hill, Massachusetts)).

SA-Bgal staining

Senescence-associated beta galactosidase (SABgal) staining was conducted following the manufacturer's protocol (Cat# 9860S, Cell Signaling Technology), with all reagents diluted in 1X PBS instead of dH2O.

Colony formation assays

Clonogenic outgrowth was performed in a 6-well plate by plating 1600, 800, and 400 cells per well using a 2× serial dilution method. First, 6400 cells were suspended in 16 mL of media, and 4 mL was plated into each of two wells (1600 cells/well). The remaining 8 mL of suspension was then diluted with an additional 8 mL of media (2X dilution), and 4 mL was plated into two more wells (800 cells/well). This dilution step was repeated once more to obtain 400 cells/well. Cells were allowed to grow for 10–12 days in drug-free media, followed by staining with crystal violet (1.25 g in 100 mL methanol and 400 mL distilled water) for 10 minutes at room temperature. Plates were washed with cold water, dried overnight, and scanned using an Epson Perfection V600 photo scanner.

RT-qPCR

Total RNA was extracted using the Quick-RNA Microprep Kit (Cat# R1050, Zymo Research) from at least two biological replicates per condition. cDNA was synthesized with the Applied Biosystems High-Capacity cDNA Reverse Transcription Kit (Cat# 4368814, Thermo Fisher Scientific) and SUPERase• In™ RNase Inhibitor (Cat# AM2696, Thermo Fisher Scientific). Prior to qPCR, cDNA was diluted to 5 ng/µL in dH2O.

qPCR was performed in triplicate in a 96-well microplate using a 15 µL reaction containing 7.5 µL PowerUp SYBR Green Master Mix (Cat# A25742, Thermo Fisher Scientific), 4 µL dH2O, 0.75 µL each of forward and reverse primers, and 1.5 µL of 5 ng/µL cDNA. Reactions were run on a QuantStudio™ 5 Real-Time PCR System with the following untreated cycling conditions: 98°C for 30 seconds, followed by 40–45 cycles of 98°C for 10 seconds, 63°C for 30 seconds, and 72°C for 1 minute. Cq values were normalized to the housekeeping gene *PUM1*, which was selected based on its stable expression across conditions in RNA-seq datasets.

QUANTIFICATION AND STATISTICAL ANALYSIS

Image quantification

All images were acquired using the Nikon Ti2E Research Microscope System where about 100 nuclei or more were used for downstream quantification. To quantify ATRX, macroH2A, γH2AX, and 53BP1 foci in immunofluorescent images, we used a custom CellProfiler pipeline.[95] Foci and nuclei were identified using the **IdentifyPrimaryObjects** module, with the **EnhanceOrSuppressFeatures** module applied beforehand to improve foci detection. The **RelateObjects** module was then used to associate foci with their respective nuclei.

The NF-κB nuclear-to-perinuclear intensity ratio was calculated using a CellProfiler pipeline based on https://www.youtube.com/watch?v=DlQSgDIGuds.

Briefly, **IdentifyPrimaryObjects** detected nuclei, followed by **ExpandOrShrinkObjects** to expand nuclear boundaries, and **IdentifyTertiaryObjects** to define the perinuclear region. The **MeasureObjectIntensity** module was then used to quantify intensity in nuclear and perinuclear regions. SABgal+ associated nuclei were manually counted using Fiji software.[96] For all quantifications, Dunnett's test was used to test for significance between pairwise comparisons of conditions.

RNA-sequencing pre-processing

Reads containing adapters, N > 10% (N represents the base cannot be determined) and low quality (Qscore<= 5) reads were filtered out. Pseudoalignment and quantification of transcripts were performed with kallisto.[97]

Differential gene expression analysis

LS8817: Downstream analysis was performed in RStudio v3.6.3. Kallisto counts were imported into R using tximport v1.14.2, and differential gene expression analysis was conducted with DESeq2 1.26.0.[98] Genes with fewer than 50 total counts across all samples were filtered out. Significantly differentially expressed genes were identified using a likelihood ratio test (*Padj* < 0.05) and a Wald test (absolute log2FC ≥ 2) relative to Cycling or day 3 treatment controls.A total of 3,744 differentially expressed genes were identified and clustered into seven RNA expression groups using k-means clustering. To characterize expression patterns across treatments, genes were further categorized as "Shared-down," "Palbo-upregulated," "Doxo-upregulated," or "Shared-up." rlog-normalized gene expression values were visualized using the pheatmap R package, with values scaled by row to enhance comparability.

MCF7: Quantification of transcripts and read alignment were performed with STAR 2.7.10a Genes with at least 1 sample with > 5 counts were kept. Differential gene expression analysis was conducted with DESeq2[98] and significantly differentially expressed genes were identified using a likelihood ratio test (*Padj* < 0.05)

Identification of SASP and transcription factor target genes

SASP genes: We used the manually curated databases provided in Wang et al.,[22] Gleason et al.,[9] and the SASPAtlas[99] (511 genes). Filtering for significantly changing genes present in all three databases, we identified 277 SASP genes that were associated with either therapy-induced senescence.

Cell cycle genes: Significantly changing genes were annotated as Cell Cycle if they were found in one of the following databases (892 genes). Hallmark: “E2F TARGETS,” “G2M_CHECKPOINT;” Reactome: “CELL_CYCLE,” “CELL_CYCLE_CHECKPOINTS,” “CELL_CYCLE_MITOTIC;” KEGG: “CELL_CYCLE.”

P53 target genes: Significantly changing genes were cross-referenced with the curated p53 target list from Fischer and the "P53 PATHWAY" Hallmark term (473 genes), identifying 102 upregulated p53 target genes across RNA clusters.

NF-κB target genes: We used the Gilmore Lab NF-κB target gene database (https://www.bu.edu/nf-kb/gene-resources/target-genes/), the "TNFA SIGNALING VIA NFKB" Hallmark term, and Ingenuity Pathway Analysis (IPA) upstream regulators containing the pattern, "NFKB" (687 genes). Filtering for significantly changing genes present in all three sources, we identified 163 upregulated NF-κB target genes across RNA clusters.

E2F target genes: We filtered significantly changing genes against the “E2F TARGETS” Hallmark term and IPA upstream regulators containing the pattern, “E2F” (291 genes), identifying 164 downregulated E2F target genes.

GO enrichment analysis

GO enrichment was performed using enricher function from clusterProfiler package,[100] using gene IDs from each RNA cluster examining MSigDB databases.[101, 102] Default settings of *P*-value cutoff = 0.05 and *P*-adjust method = “BH” were used. Background gene set for GO enrichment was set as all genes expressed. -log10(*Padj*) values for the top 5-10 enriched terms across all databases for each RNA cluster were plotted as a heatmap using pheatmap R package.

GSEA analysis

Genes were ranked based on the product of log2FC*-log10(*P*-value), from DESeq2 results. GSEA was performed on the ranked list of genes using the GSEA function from clusterProfiler package v3.14.3 using the default settings.[103] Running enrichment score plots were generated using the gseaplot function with the setting “by = runningScore.”

Ingenuity Pathway Analysis

To determine predicted upstream regulators, data were analyzed with the use of QIAGEN IPA (QIAGEN Inc., https://digitalinsights.qiagen.com/IPA) where the core analysis was performed on gene IDs from each RNA cluster.[104] To determine the activation scores and visualize predicted relationships between upstream regulators,

IPA core analysis was performed on log2FC values of gene IDs across timepoints relative to Cycling or day 3 treatment controls with a threshold set to an absolute value of log2FC = 1.

To identify differentially activated upstream regulators and compare between drugs, an IPA comparison was performed on the individual core analyses results, generating a matrix of activation scores. To filter for the top 10-12 most differentially activated upstream regulators, the sum of activation scores across timepoints within each drug was calculated. Upstream regulators with activation scores significantly higher in one treatment condition relative to the other were selected based on greatest magnitude differences between drugs. Conversely, upstream regulators significantly activated in Doxo-treated conditions but repressed in Palbo-treated conditions were selected based on an analogous threshold.

To identify the top activated or inhibited upstream regulators for each drug treatment overall, the sum of activation scores across multiple conditions within drug was ranked from highest to lowest.

For all analyses, filtered upstream regulators were cross-referenced with a list of expressed genes in this cell line to ensure biological relevance. -log10(*Padj*) values for the top 5-10 enriched upstream regulators or activation scores for each condition were plotted as a heatmap using pheatmap R package.

CUT&Tag preprocessing

The preprocessing of CUT&Tag data, including alignment of FASTQ into BAM files, and the generation of BigWig files, was performed as previously described.[94]

ATAC-sequencing preprocessing

Adapters were trimmed using cutadapt and reads were aligned with bowtie2 to the hg38 genome. Following this, duplicate reads and reads mapping to the mitochondrial genome were removed. BAM files were converted to bedpe files, which were then converted to tagAlign files for MACS2 to call peaks on, areas of the genome enriched for aligned sequencing reads, indicating hyper-accessibility. MACS2 parameters were `-g 2.7e9 -p 0.2 --shift -75 --extsize 150 --nomodel -B --SPMR --keep-dup all --call-summits`. Reproducible peaks across technical replicates per condition were kept using Irreproducible Discovery Rate.[105] A master nonredundant peak set was generated using a custom iterative peak filtering script which selects the peak with the lowest q-value generated by MACS2 from a set of overlapping peaks. Peaks were fixed to 500 bp in length, with 250 bp extending from the summit identified by MACS2.[106] In total we identified 215,671 non-redundant peaks. Fragment counts under peaks were counted using chromVAR's `getCounts` function.[107]

ATAC-seq fragment length distribution:

Biological replicates per condition were merged into a single BAM file using samtools merge function.[108] The following line of code was used to extract the fragment length and count the number of unique occurrences for each fragment length: `samtools view $INPUT| awk -F'\t' 'function abs(x)(return ((x < 0.0) ? -x : x)) (print abs($9))' | sort -n | uniq -c | awk -v OFS="\t" '(print $2, $1/2)' >$OUTPUT\_insertdata.txt` where $INPUT is the merged BAM file and $OUTPUT is the directory path and file name. The output text file containing fragment length information was imported into R. The overall fragment length distribution was normalized by dividing the number of each fragment length by the total number of fragments in the merged BAM file. The resulting fragment length distribution was plotted using ggplot2 v3.5.1 package in R as a line plot.

Differential ATAC-seq peak analysis

Differential peak analysis was performed using DESeq2 with the Wald test, based on pairwise comparisons of each timepoint relative to Cycling or day 3 treatment controls. Among the 215,671 unique peaks in our non-redundant master peak set, we identified 49,107 upregulated and 42,164 downregulated peaks across both drug treatments. Peaks were considered significant based on a Bonferroni-corrected *Padj* threshold (0.01/215,671 total peaks) and an absolute log2FC > 1 at any timepoint compared to Cycling or day 3 treatment controls. Upregulated peaks were categorized as "Doxo-upregulated" if they were significant in Doxo but not Palbo, "Palbo-upregulated" if significant in Palbo but not Doxo, and "Shared-upregulated" if significant in both treatments. The same criteria were applied for categorizing downregulated peaks.

To visualize read counts under significantly upregulated peaks, reads were variance-stabilizing transformed (VST) and ordered based on their classification as Palbo-upregulated, Shared-upregulated, or Doxo-upregulated. Hierarchical clustering was applied within each drug category to improve the coherence of the heatmap structure. VST-normalized counts were visualized using the pheatmap package, with values scaled across rows to enhance comparability. The same was performed for downregulated peaks.

Peak Annotation

Significantly changing peaks at each timepoint relative to Cycling or day 3 treatment controls within each drug were merged into a single peak set. Peaks were annotated using the `annotatePeak` function from ChIPseeker with the UCSC hg38 knownGene TxDb.[109] For easier visualization of heatmap of reads under peaks, categories “Exon”, “Intron”, “3’ UTR” and “5’ UTR” were merged into a single “Gene Body category” and categories “Distal intergenic” and “Downstream” were merged into a single “Distal” category.

Nearby peaks identification

Genomic coordinates of genes were obtained from the comprehensive gene annotation file in GENCODE Release 41 (GRCh38.p13).[110] For each RNA cluster of significantly changing genes, gene boundaries were extended by 50 kb upstream and downstream. Significantly changing peaks were then filtered to retain those overlapping with the extended genomic coordinates of each RNA cluster. Additionally, nearby static peaks (peaks that did not meet the significance criteria) were identified using the same approach.

Motif enrichment analysis

Motif enrichment analysis was performed using Analysis of Motif Enrichment (AME) from the MEME SUITE v5.0.2.[111] Enriched motifs were identified under peaks using the HOCOMOCO v11 database with the following command: `ame --verbose 1 --scoring avg --method fisher --hit-lo-fraction 0.25 --evalue-report-threshold 10.0 --control $CONTROL --kmer 2 $INPUT HOCOMOCOv11_core_HUMAN_mono_meme_format.meme.`

Here $CONTROL represents the FASTA file containing sequences from background peaks, and $INPUT contains sequences from foreground peaks.

For motif enrichment analysis in upregulated peaks, FASTA sequences were extracted from upregulated peaks at each time point relative to either Cycling (untreated) or day 3-treated controls within each drug treatment; these were used as the foreground peak set, with the corresponding downregulated peaks serving as the background set. The same approach while switching the foreground and background sets was used to identify motifs enriched in downregulated peaks.

To determine differentially enriched motifs between Palbo- and Doxo-upregulated peaks, Palbo-upregulated peaks were used as the foreground set, while Doxo-upregulated peaks served as the background set, and vice versa.

For motif enrichment in nearby peaks of RNA clusters, up- or downregulated nearby peaks for each drug treatment were used as the foreground set, while static nearby peaks served as the background set.

Motif enrichment results were visualized as heatmaps of -log10(*Padj*) values using the pheatmap R package or as dot plots displaying %True Positive – %False Positive and -log10(*Padj*) values using ggplot2 v3.5.1.

ATAC-seq coverage plots

Tn5 insertion sites were identified as fragment ends from merged BAM files of biological replicates for each condition and saved as bigWig files. This was performed in R using a custom script. In brief, the `resize` and `shift` functions in GenomicRanges were used to retain and shift the ends of reads to +4, -5 bp to account for Tn5 insertion bias. The `coverage` function was used to convert the fragment ends into a RleList object. To

normalize bigWig files, reads were counted in 500 bp bins tiled across the genome, and the resulting count matrix was used in DESeq to calculate size factors with the `estimateSizeFactors` function. Normalization was performed by multiplying the coverage by a scale factor (1/DESeq size factor) before exporting the resulting object as a bigWig.

For accessibility signal plots around motifs, motif genomic coordinates were identified using position weight matrices from HOCOMOCO v11 and scanned across the hg38 genome with motifmatchr 1.8.0.[112] Motifs overlapping up- or downregulated peaks at any time point for each drug category (Doxo, Shared, Palbo) were saved as BED files and used for coverage plotting in deepTools.[113] The same approach was applied to nearby peaks of RNA cluster peak sets. Tn5 insertion site coverage was plotted within 1 kb of motifs using deepTools with the `computeMatrix` function (`--referencePoint center`) and `plotProfile` function.

For transcription start site (TSS) accessibility, the same method was used with a BED file of genes from GENCODE Release 41 (GRCh38.p13),[110] applying `computeMatrix (--referencePoint TSS)` and `plotProfile` in deepTools.

Genome browser visualization

Normalized bigwigs were generated from merged BAM files of biological replicates for each condition using the `bamCoverage` function from deepTools with the following command: `bamCoverage -b $INPUT -o $OUTPUT --binSize 5 --scaleFactor $SCALE --extendReads` where $INPUT is the merged BAM file and $OUTPUT is the resulting bigwig file. $SCALE is the same scale factor used to generate bigWigs for fragment ends. BigWigs were then visualized on Integrative Genomics Viewer (IGV).

Visualization of geneHancer data of putative connected enhancers linked to NF-κB target genes was achieved by converting geneHancer v5.20 gff file to a bedpe file and filtering for geneHancers that had at least one NF-κB target gene as the connected gene ID.[114] Putative RelA binding sites were derived from the cis-regulatory modules (CRMs) ReMap 2022 database.[115]

Sample distance and PCA

Distance measures between samples were calculated by using the `dist` function on the transposed VST-normalized counts matrix for ATAC-seq or rlog-normalized counts matrix for RNA-seq in R. Prior to this, technical replicates were merged into biological replicates for ATAC-seq. The resulting distance values were plotted using pheatmap. Principal component analysis (PCA) plots were generated using DESeq2's `plotPCA` function.

COMPETING INTERESTS

A. K. reports grants from NIH, NCI, Jennifer Linn Fund Cycle for Survival, The Maloris Foundation, and Sarcoma Foundation of America and other support from Eli Lilly during the conduct of the study as well as personal fees from Eli Lilly, Concarlo Therapeutics, and PTT Global Chemical; grants from Eli Lilly and Novartis; and other support from Atropos Therapeutics outside the submitted work. In addition, A. K. has a patent for US9889135 issued. V. I. R. has submitted a patent application (PCT/US2024/059554) for a chromatin conformation capture method.

REFERENCES

1. Di Micco R, Krizhanovsky V, Baker D, d'Adda di Fagagna F. Cellular senescence in ageing: from mechanisms to therapeutic opportunities. *Nat Rev Mol Cell Biol* 2021, **22**(2)**:** 75–95.

2. d'Adda di Fagagna F. Living on a break: cellular senescence as a DNA-damage response. *Nat Rev Cancer* 2008, **8**(7)**:** 512–522.

3. Campisi J. Senescent cells, tumor suppression, and organismal aging: good citizens, bad neighbors. *Cell* 2005, **120**(4)**:** 513–522.

4. Blagosklonny MV. Geroconversion: irreversible step to cellular senescence. *Cell Cycle* 2014, **13**(23)**:** 3628–3635.

5. Sheekey E, Narita M. p53 in senescence - it's a marathon, not a sprint. *FEBS J* 2023, **290**(5)**:** 1212–1220.

6. Torres G, Salladay-Perez IA, Dhingra A, Covarrubias AJ. Genetic origins, regulators, and biomarkers of cellular senescence. *Trends Genet* 2024, **40**(12)**:** 1018–1031.

7. Klein ME, Kovatcheva M, Davis LE, Tap WD, Koff A. CDK4/6 Inhibitors: The Mechanism of Action May Not Be as Simple as Once Thought. *Cancer Cell* 2018, **34**(1)**:** 9–20.

8. Guan X, LaPak KM, Hennessey RC, Yu CY, Shakya R, Zhang J*, et al.* Stromal Senescence By Prolonged CDK4/6 Inhibition Potentiates Tumor Growth. *Mol Cancer Res* 2017, **15**(3)**:** 237–249.

9. Gleason CE, Dickson MA, Klein Dooley ME, Antonescu CR, Gularte-Merida R, Benitez M*, et al.* Therapy-Induced Senescence Contributes to the Efficacy of Abemaciclib in Patients with Dedifferentiated Liposarcoma. *Clin Cancer Res* 2024, **30**(4)**:** 703–718.

10. Wagner V, Gil J. Senescence as a therapeutically relevant response to CDK4/6 inhibitors. *Oncogene* 2020, **39**(29)**:** 5165–5176.

11. Malaquin N, Martinez A, Rodier F. Keeping the senescence secretome under control: Molecular reins on the senescence-associated secretory phenotype. *Exp Gerontol* 2016, **82:** 39–49.

12. Hernandez-Segura A, Nehme J, Demaria M. Hallmarks of Cellular Senescence. *Trends Cell Biol* 2018, **28**(6)**:** 436–453.

13. Wang B, Han J, Elisseeff JH, Demaria M. The senescence-associated secretory phenotype and its physiological and pathological implications. *Nat Rev Mol Cell Biol* 2024, **25**(12)**:** 958–978.

14. Suryadevara V, Hudgins AD, Rajesh A, Pappalardo A, Karpova A, Dey AK*, et al.* SenNet recommendations for detecting senescent cells in different tissues. *Nat Rev Mol Cell Biol* 2024, **25**(12)**:** 1001–1023.

15. Chambers CR, Ritchie S, Pereira BA, Timpson P. Overcoming the senescence-associated secretory phenotype (SASP): a complex mechanism of resistance in the treatment of cancer. *Mol Oncol* 2021, **15**(12)**:** 3242–3255.

16. Faget DV, Ren Q, Stewart SA. Unmasking senescence: context-dependent effects of SASP in cancer. *Nat Rev Cancer* 2019, **19**(8)**:** 439–453.

17. Lau L, David G. Pro- and anti-tumorigenic functions of the senescence-associated secretory phenotype. *Expert Opin Ther Targets* 2019, **23**(12)**:** 1041–1051.

18. Chien Y, Scuoppo C, Wang X, Fang X, Balgley B, Bolden JE*, et al.* Control of the senescence-associated secretory phenotype by NF-kappaB promotes senescence and enhances chemosensitivity. *Genes Dev* 2011, **25**(20)**:** 2125–2136.

19. Salminen A, Kauppinen A, Kaarniranta K. Emerging role of NF-kappaB signaling in the induction of senescence-associated secretory phenotype (SASP). *Cell Signal* 2012, **24**(4)**:** 835–845.

20. Goel S, DeCristo MJ, Watt AC, BrinJones H, Sceneay J, Li BB*, et al.* CDK4/6 inhibition triggers anti-tumour immunity. *Nature* 2017, **548**(7668)**:** 471–475.

21. Lee DH, Imran M, Choi JH, Park YJ, Kim YH, Min S*, et al.* CDK4/6 inhibitors induce breast cancer senescence with enhanced anti-tumor immunogenic properties compared with DNA-damaging agents. *Mol Oncol* 2024, **18**(1)**:** 216–232.

22. Wang B, Varela-Eirin M, Brandenburg SM, Hernandez-Segura A, van Vliet T, Jongbloed EM*, et al.* Pharmacological CDK4/6 inhibition reveals a p53-dependent senescent state with restricted toxicity. *EMBO J* 2022, **41**(6)**:** e108946.

23. Lee S, Schmitt CA. The dynamic nature of senescence in cancer. *Nat Cell Biol* 2019, **21**(1)**:** 94–101.

24. Patnaik A, Rosen LS, Tolaney SM, Tolcher AW, Goldman JW, Gandhi L*, et al.* Efficacy and Safety of Abemaciclib, an Inhibitor of CDK4 and CDK6, for Patients with Breast Cancer, Non-Small Cell Lung Cancer, and Other Solid Tumors. *Cancer Discov* 2016, **6**(7)**:** 740–753.

25. Dickson MA, Schwartz GK, Keohan ML, D'Angelo SP, Gounder MM, Chi P*, et al.* Progression-Free Survival Among Patients With Well-Differentiated or Dedifferentiated Liposarcoma Treated With CDK4 Inhibitor Palbociclib: A Phase 2 Clinical Trial. *JAMA Oncol* 2016, **2**(7)**:** 937–940.

26. Haddox CL, Hornick JL, Roland CL, Baldini EH, Keedy VL, Riedel RF. Diagnosis and management of dedifferentiated liposarcoma: A multidisciplinary position statement. *Cancer Treat Rev* 2024, **131:** 102846.

27. Reddy PM, Martin JM, Montero AJ. CDK 4/6 Inhibitors: Evolution and Revolution in the Management of ER+ Metastatic Breast Cancer. *JCO Oncol Pract* 2022, **18**(5)**:** 329–330.

28. Wang X, Zhao S, Xin Q, Zhang Y, Wang K, Li M. Recent progress of CDK4/6 inhibitors' current practice in breast cancer. *Cancer Gene Ther* 2024, **31**(9)**:** 1283–1291.

29. Toettcher J. Cell Cycle Arrest After DNA Damage. In: Dubitzky W, Wolkenhauer O, Cho K-H, Yokota H (eds). *Encyclopedia of Systems Biology*. Springer New York: New York, NY, 2013, pp 249–254.

30. Crago AM, Singer S. Clinical and molecular approaches to well differentiated and dedifferentiated liposarcoma. *Curr Opin Oncol* 2011, **23**(4)**:** 373–378.

31. Tan MC, Brennan MF, Kuk D, Agaram NP, Antonescu CR, Qin LX*, et al.* Histology-based Classification Predicts Pattern of Recurrence and Improves Risk Stratification in Primary Retroperitoneal Sarcoma. *Ann Surg* 2016, **263**(3)**:** 593–600.

32. Jolissaint JS, Raut CP, Fairweather M. Management of Recurrent Retroperitoneal Sarcoma. *Curr Oncol* 2023, **30**(3)**:** 2761–2769.

33. Knebel C, Lenze U, Pohlig F, Lenze F, Harrasser N, Suren C*, et al.* Prognostic factors and outcome of Liposarcoma patients: a retrospective evaluation over 15 years. *BMC Cancer* 2017, **17**(1)**:** 410.

34. Hsu JY, Seligson ND, Hays JL, Miles WO, Chen JL. Clinical Utility of CDK4/6 Inhibitors in Sarcoma: Successes and Future Challenges. *JCO Precis Oncol* 2022, **6:** e2100211.

35. Kovatcheva M, Liao W, Klein ME, Robine N, Geiger H, Crago AM*, et al.* ATRX is a regulator of therapy induced senescence in human cells. *Nat Commun* 2017, **8**(1)**:** 386.

36. Zhang R, Poustovoitov MV, Ye X, Santos HA, Chen W, Daganzo SM*, et al.* Formation of MacroH2A-containing senescence-associated heterochromatin foci and senescence driven by ASF1a and HIRA. *Dev Cell* 2005, **8**(1)**:** 19–30.

37. Kciuk M, Gielecińska A, Mujwar S, Kołat D, Kałuzińska-Kołat Ż, Celik I*, et al.* Doxorubicin-An Agent with Multiple Mechanisms of Anticancer Activity. *Cells* 2023, **12**(4).

38. Watt AC, Goel S. Cellular mechanisms underlying response and resistance to CDK4/6 inhibitors in the treatment of hormone receptor-positive breast cancer. *Breast Cancer Res* 2022, **24**(1)**:** 17.

39. Linders AN, Dias IB, López Fernández T, Tocchetti CG, Bomer N, Van der Meer P. A review of the pathophysiological mechanisms of doxorubicin-induced cardiotoxicity and aging. *NPJ Aging* 2024, **10**(1)**:** 9.

40. Chandra T, Ewels PA, Schoenfelder S, Furlan-Magaril M, Wingett SW, Kirschner K*, et al.* Global reorganization of the nuclear landscape in senescent cells. *Cell Rep* 2015, **10**(4)**:** 471–483.

41. Dasgupta N, Arnold R, Equey A, Gandhi A, Adams PD. The role of the dynamic epigenetic landscape in senescence: orchestrating SASP expression. *NPJ Aging* 2024, **10**(1)**:** 48.

42. Swanson EC, Manning B, Zhang H, Lawrence JB. Higher-order unfolding of satellite heterochromatin is a consistent and early event in cell senescence. *J Cell Biol* 2013, **203**(6)**:** 929–942.

43. Watt AC, Cejas P, DeCristo MJ, Metzger-Filho O, Lam EYN, Qiu X*, et al.* CDK4/6 inhibition reprograms the breast cancer enhancer landscape by stimulating AP-1 transcriptional activity. *Nat Cancer* 2021, **2**(1)**:** 34–48.

44. Martínez-Zamudio RI, Roux PF, de Freitas JANL, Robinson L, Doré G, Sun B*, et al.* AP-1 imprints a reversible transcriptional programme of senescent cells. *Nat Cell Biol* 2020, **22**(7)**:** 842–855.

45. Ren Q, Liu Z, Wu L, Yin G, Xie X, Kong W*, et al.* C/EBPβ: The structure, regulation, and its roles in inflammation-related diseases. *Biomed Pharmacother* 2023, **169:** 115938.

46. Awasthi N, Liongue C, Ward AC. STAT proteins: a kaleidoscope of canonical and non-canonical functions in immunity and cancer. *J Hematol Oncol* 2021, **14**(1)**:** 198.

47. Sarkar A, Hochedlinger K. The sox family of transcription factors: versatile regulators of stem and progenitor cell fate. *Cell Stem Cell* 2013, **12**(1)**:** 15–30.

48. Currey L, Thor S, Piper M. TEAD family transcription factors in development and disease. *Development* 2021, **148**(12).

49. Huh HD, Kim DH, Jeong HS, Park HW. Regulation of TEAD Transcription Factors in Cancer Biology. *Cells* 2019, **8**(6).

50. Romano O, Miccio A. GATA factor transcriptional activity: Insights from genome-wide binding profiles. *IUBMB Life* 2020, **72**(1)**:** 10–26.

51. Golson ML, Kaestner KH. Fox transcription factors: from development to disease. *Development* 2016, **143**(24)**:** 4558–4570.

52. Balamurugan K, Sterneck E. The many faces of C/EBPδ and their relevance for inflammation and cancer. *Int J Biol Sci* 2013, **9**(9)**:** 917–933.

53. Kamachi Y, Kondoh H. Sox proteins: regulators of cell fate specification and differentiation. *Development* 2013, **140**(20)**:** 4129–4144.

54. Tremblay M, Sanchez-Ferras O, Bouchard M. GATA transcription factors in development and disease. *Development* 2018, **145**(20).

55. Li YJ, Zhang C, Martincuks A, Herrmann A, Yu H. STAT proteins in cancer: orchestration of metabolism. *Nat Rev Cancer* 2023, **23**(3)**:** 115–134.

56. Fischer M. Census and evaluation of p53 target genes. *Oncogene* 2017, **36**(28)**:** 3943–3956.

57. Blokzijl A, ten Dijke P, Ibáñez CF. Physical and functional interaction between GATA-3 and Smad3 allows TGF-beta regulation of GATA target genes. *Curr Biol* 2002, **12**(1)**:** 35–45.

58. Gomis RR, Alarcón C, Nadal C, Van Poznak C, Massagué J. C/EBPbeta at the core of the TGFbeta cytostatic response and its evasion in metastatic breast cancer cells. *Cancer Cell* 2006, **10**(3)**:** 203–214.

59. Liu D, Kang JS, Derynck R. TGF-beta-activated Smad3 represses MEF2-dependent transcription in myogenic differentiation. *EMBO J* 2004, **23**(7)**:** 1557–1566.

60. Qiao Y, Wang Z, Tan F, Chen J, Lin J, Yang J*, et al.* Enhancer Reprogramming within Pre-existing Topologically Associated Domains Promotes TGF-β-Induced EMT and Cancer Metastasis. *Mol Ther* 2020, **28**(9)**:** 2083–2095.

61. Yu W, Huang C, Wang Q, Huang T, Ding Y, Ma C*, et al.* MEF2 transcription factors promotes EMT and invasiveness of hepatocellular carcinoma through TGF-β1 autoregulation circuitry. *Tumour Biol* 2014, **35**(11)**:** 10943–10951.

62. Kuwahara M, Yamashita M, Shinoda K, Tofukuji S, Onodera A, Shinnakasu R*, et al.* The transcription factor Sox4 is a downstream target of signaling by the cytokine TGF-β and suppresses T(H)2 differentiation. *Nat Immunol* 2012, **13**(8)**:** 778–786.

63. Hu J, Tian J, Zhu S, Sun L, Yu J, Tian H*, et al.* Sox5 contributes to prostate cancer metastasis and is a master regulator of TGF-β-induced epithelial mesenchymal transition through controlling Twist1 expression. *Br J Cancer* 2018, **118**(1)**:** 88–97.

64. Han Y, Lefebvre V. L-Sox5 and Sox6 drive expression of the aggrecan gene in cartilage by securing binding of Sox9 to a far-upstream enhancer. *Mol Cell Biol* 2008, **28**(16)**:** 4999–5013.

65. Brill E, Gobble R, Angeles C, Lagos-Quintana M, Crago A, Laxa B*, et al.* ZIC1 overexpression is oncogenic in liposarcoma. *Cancer Res* 2010, **70**(17)**:** 6891–6901.

66. Liu T, Zhang L, Joo D, Sun SC. NF-κB signaling in inflammation. *Signal Transduct Target Ther* 2017, **2:** 17023–.

67. Viatour P, Merville MP, Bours V, Chariot A. Phosphorylation of NF-kappaB and IkappaB proteins: implications in cancer and inflammation. *Trends Biochem Sci* 2005, **30**(1)**:** 43–52.

68. Pierce JW, Schoenleber R, Jesmok G, Best J, Moore SA, Collins T*, et al.* Novel inhibitors of cytokine-induced IkappaBalpha phosphorylation and endothelial cell adhesion molecule expression show anti-inflammatory effects in vivo. *J Biol Chem* 1997, **272**(34)**:** 21096–21103.

69. Lau L, Porciuncula A, Yu A, Iwakura Y, David G. Uncoupling the Senescence-Associated Secretory Phenotype from Cell Cycle Exit via Interleukin-1 Inactivation Unveils Its Protumorigenic Role. *Mol Cell Biol* 2019, **39**(12).

70. Birch J, Gil J. Senescence and the SASP: many therapeutic avenues. *Genes Dev* 2020, **34**(23-24)**:** 1565–1576.

71. Schmitt CA, Wang B, Demaria M. Senescence and cancer - role and therapeutic opportunities. *Nat Rev Clin Oncol* 2022, **19**(10)**:** 619–636.

72. Kurppa KJ, Liu Y, To C, Zhang T, Fan M, Vajdi A*, et al.* Treatment-Induced Tumor Dormancy through YAP-Mediated Transcriptional Reprogramming of the Apoptotic Pathway. *Cancer Cell* 2020, **37**(1)**:** 104–122.e112.

73. McHugh D, Gil J. Senescence and aging: Causes, consequences, and therapeutic avenues. *J Cell Biol* 2018, **217**(1)**:** 65–77.

74. Wang B, Kohli J, Demaria M. Senescent Cells in Cancer Therapy: Friends or Foes? *Trends Cancer* 2020, **6**(10)**:** 838–857.

75. Crozier L, Foy R, Adib R, Kar A, Holt JA, Pareri AU*, et al.* CDK4/6 inhibitor-mediated cell overgrowth triggers osmotic and replication stress to promote senescence. *Mol Cell* 2023, **83**(22)**:** 4062–4077 e4065.

76. Crozier L, Foy R, Mouery BL, Whitaker RH, Corno A, Spanos C*, et al.* CDK4/6 inhibitors induce replication stress to cause long-term cell cycle withdrawal. *EMBO J* 2022, **41**(6)**:** e108599.

77. Rodier F, Coppe JP, Patil CK, Hoeijmakers WA, Munoz DP, Raza SR*, et al.* Persistent DNA damage signalling triggers senescence-associated inflammatory cytokine secretion. *Nat Cell Biol* 2009, **11**(8)**:** 973–979.

78. Fujioka S, Niu J, Schmidt C, Sclabas GM, Peng B, Uwagawa T*, et al.* NF-kappaB and AP-1 connection: mechanism of NF-kappaB-dependent regulation of AP-1 activity. *Mol Cell Biol* 2004, **24**(17)**:** 7806–7819.

79. Ji Z, He L, Regev A, Struhl K. Inflammatory regulatory network mediated by the joint action of NF-kB, STAT3, and AP-1 factors is involved in many human cancers. *Proc Natl Acad Sci U S A* 2019, **116**(19)**:** 9453–9462.

80. Oeckinghaus A, Hayden MS, Ghosh S. Crosstalk in NF-kappaB signaling pathways. *Nat Immunol* 2011, **12**(8)**:** 695–708.

81. Ancrile B, Lim KH, Counter CM. Oncogenic Ras-induced secretion of IL6 is required for tumorigenesis. *Genes Dev* 2007, **21**(14)**:** 1714–1719.

82. Acosta JC, Gil J. A role for CXCR2 in senescence, but what about in cancer? *Cancer Res* 2009, **69**(6)**:** 2167–2170.

83. Jones SA, Jenkins BJ. Recent insights into targeting the IL-6 cytokine family in inflammatory diseases and cancer. *Nat Rev Immunol* 2018, **18**(12)**:** 773–789.

84. Rebe C, Ghiringhelli F. Interleukin-1beta and Cancer. *Cancers (Basel)* 2020, **12**(7).

85. Garlanda C, Mantovani A. Interleukin-1 in tumor progression, therapy, and prevention. *Cancer Cell* 2021, **39**(8)**:** 1023–1027.

86. Wu T, Yang W, Sun A, Wei Z, Lin Q. The Role of CXC Chemokines in Cancer Progression. *Cancers (Basel)* 2022, **15**(1).

87. Kovatcheva M, Liu DD, Dickson MA, Klein ME, O'Connor R, Wilder FO*, et al.* MDM2 turnover and expression of ATRX determine the choice between quiescence and senescence in response to CDK4 inhibition. *Oncotarget* 2015, **6**(10)**:** 8226–8243.

88. Gobble RM, Qin LX, Brill ER, Angeles CV, Ugras S, O'Connor RB*, et al.* Expression profiling of liposarcoma yields a multigene predictor of patient outcome and identifies genes that contribute to liposarcomagenesis. *Cancer Res* 2011, **71**(7)**:** 2697–2705.

89. Miller ML, Molinelli EJ, Nair JS, Sheikh T, Samy R, Jing X*, et al.* Drug synergy screen and network modeling in dedifferentiated liposarcoma identifies CDK4 and IGF1R as synergistic drug targets. *Sci Signal* 2013, **6**(294)**:** ra85.

90. Barretina J, Taylor BS, Banerji S, Ramos AH, Lagos-Quintana M, Decarolis PL*, et al.* Subtype-specific genomic alterations define new targets for soft-tissue sarcoma therapy. *Nat Genet* 2010, **42**(8)**:** 715–721.

91. Singer S, Socci ND, Ambrosini G, Sambol E, Decarolis P, Wu Y*, et al.* Gene expression profiling of liposarcoma identifies distinct biological types/subtypes and potential therapeutic targets in well-differentiated and dedifferentiated liposarcoma. *Cancer Res* 2007, **67**(14)**:** 6626–6636.

92. Corces MR, Trevino AE, Hamilton EG, Greenside PG, Sinnott-Armstrong NA, Vesuna S*, et al.* An improved ATAC-seq protocol reduces background and enables interrogation of frozen tissues. *Nat Methods* 2017, **14**(10)**:** 959–962.

93. Kaya-Okur HS, Janssens DH, Henikoff JG, Ahmad K, Henikoff S. Efficient low-cost chromatin profiling with CUT&Tag. *Nat Protoc* 2020, **15**(10)**:** 3264–3283.

94. Soroczynski J, Anderson LJ, Yeung JL, Rendleman JM, Oren DA, Konishi HA*, et al.* OpenTn5: Open-Source Resource for Robust and Scalable Tn5 Transposase Purification and Characterization. *bioRxiv* 2024.

95. Stirling DR, Swain-Bowden MJ, Lucas AM, Carpenter AE, Cimini BA, Goodman A. CellProfiler 4: improvements in speed, utility and usability. *BMC Bioinformatics* 2021, **22**(1)**:** 433.

96. Schindelin J, Arganda-Carreras I, Frise E, Kaynig V, Longair M, Pietzsch T*, et al.* Fiji: an open-source platform for biological-image analysis. *Nat Methods* 2012, **9**(7)**:** 676–682.

97. Bray NL, Pimentel H, Melsted P, Pachter L. Near-optimal probabilistic RNA-seq quantification. *Nat Biotechnol* 2016, **34**(5)**:** 525–527.

98. Love MI, Huber W, Anders S. Moderated estimation of fold change and dispersion for RNA-seq data with DESeq2. *Genome Biol* 2014, **15**(12)**:** 550.

99. Basisty N, Kale A, Jeon OH, Kuehnemann C, Payne T, Rao C*, et al.* A proteomic atlas of senescence-associated secretomes for aging biomarker development. *PLoS Biol* 2020, **18**(1)**:** e3000599.

100. Yu G, Wang LG, Han Y, He QY. clusterProfiler: an R package for comparing biological themes among gene clusters. *OMICS* 2012, **16**(5)**:** 284–287.

101. Liberzon A, Subramanian A, Pinchback R, Thorvaldsdóttir H, Tamayo P, Mesirov JP. Molecular signatures database (MSigDB) 3.0. *Bioinformatics* 2011, **27**(12)**:** 1739–1740.

102. Liberzon A, Birger C, Thorvaldsdóttir H, Ghandi M, Mesirov JP, Tamayo P. The Molecular Signatures Database (MSigDB) hallmark gene set collection. *Cell Syst* 2015, **1**(6)**:** 417–425.

103. Subramanian A, Tamayo P, Mootha VK, Mukherjee S, Ebert BL, Gillette MA*, et al.* Gene set enrichment analysis: a knowledge-based approach for interpreting genome-wide expression profiles. *Proc Natl Acad Sci U S A* 2005, **102**(43)**:** 15545–15550.

104. Krämer A, Green J, Pollard J, Tugendreich S. Causal analysis approaches in Ingenuity Pathway Analysis. *Bioinformatics* 2014, **30**(4)**:** 523–530.

105. Li Q, Brown JB, Huang H, Bickel PJ. Measuring reproducibility of high-throughput experiments. *The Annals of Applied Statistics* 2011, **5**(3)**:** 1752–1779, 1728.

106. Zhang Y, Liu T, Meyer CA, Eeckhoute J, Johnson DS, Bernstein BE*, et al.* Model-based analysis of ChIP-Seq (MACS). *Genome Biol* 2008, **9**(9)**:** R137.

107. Schep AN, Wu B, Buenrostro JD, Greenleaf WJ. chromVAR: inferring transcription-factor-associated accessibility from single-cell epigenomic data. *Nat Methods* 2017, **14**(10)**:** 975–978.

108. Li H, Handsaker B, Wysoker A, Fennell T, Ruan J, Homer N*, et al.* The Sequence Alignment/Map format and SAMtools. *Bioinformatics* 2009, **25**(16)**:** 2078–2079.

109. Yu G, Wang LG, He QY. ChIPseeker: an R/Bioconductor package for ChIP peak annotation, comparison and visualization. *Bioinformatics* 2015, **31**(14)**:** 2382–2383.

110. Frankish A, Diekhans M, Ferreira AM, Johnson R, Jungreis I, Loveland J*, et al.* GENCODE reference annotation for the human and mouse genomes. *Nucleic Acids Res* 2019, **47**(D1)**:** D766–D773.

111. McLeay RC, Bailey TL. Motif Enrichment Analysis: a unified framework and an evaluation on ChIP data. *BMC Bioinformatics* 2010, **11:** 165.

112. Kulakovskiy IV, Vorontsov IE, Yevshin IS, Sharipov RN, Fedorova AD, Rumynskiy EI*, et al.* HOCOMOCO: towards a complete collection of transcription factor binding models for human and mouse via large-scale ChIP-Seq analysis. *Nucleic Acids Res* 2018, **46**(D1)**:** D252–D259.

113. Ramírez F, Ryan DP, Grüning B, Bhardwaj V, Kilpert F, Richter AS*, et al.* deepTools2: a next generation web server for deep-sequencing data analysis. *Nucleic Acids Res* 2016, **44**(W1)**:** W160–165.

114. Fishilevich S, Nudel R, Rappaport N, Hadar R, Plaschkes I, Iny Stein T*, et al.* GeneHancer: genome-wide integration of enhancers and target genes in GeneCards. *Database (Oxford)* 2017, **2017**.

115. Hammal F, de Langen P, Bergon A, Lopez F, Ballester B. ReMap 2022: a database of Human, Mouse, Drosophila and Arabidopsis regulatory regions from an integrative analysis of DNA-binding sequencing experiments. *Nucleic Acids Res* 2022, **50**(D1)**:** D316–D325.

FIGURE LEGENDS

Figure 1: CDK4/6i and doxorubicin both induce senescence features with distinct DNA damage levels

A. Diagram summarizing CDK4/6i (Palbo) vs. doxorubicin (Doxo) mechanisms of cell cycle arrest.
B. Experimental design of drug comparison time course.
C. Left: Percent nuclei counted that had cellular SABgal+ staining at different timepoints. Number of nuclei counted was > 300 per condition at 10x magnification. Each point represents a field of view, with different shapes indicating biological replicates. Error bars denote standard deviation. Statistical significance was calculated using Dunnett's test. Right: Representative SABgal staining images at day 3 and day 14 shown at 10x magnification with scale bar = 50 µm.
D. Crystal violet staining after clonogenic outgrowth for 10-12 days. 800 cells were seeded per well in a 6-well plate in drug-free media after completion of drug treatment at each timepoint.
E. Number of ATRX foci (left) and macroH2A foci (indicative of SAHFs; middle) per nucleus was counted for ~100 nuclei per timepoint. Representative images are shown at day 14 of each drug treatment at 60x magnification (right). Significance was calculated using Dunnett's test. The scale bar is 15 µm.
F. Number of γH2AX foci (indicative of DNA damage; left) & 53BP1 foci (indicative of DNA repair; middle) per nucleus was counted for ~100 nuclei per timepoint & categorized in 0-4, 5-10 or >10 foci/nuclei. Representative images are shown at day 14 of each drug treatment at 60x magnification (right). The scale bar is 15 µm.

Figure 2: Distinct and shared transcriptional and chromatin responses define drug-specific senescence trajectories

A. Distance measures between samples ordered by treatment and timepoint.
B. Principal component analysis on RNA-seq and ATAC-seq samples.
C. K-means clustered heatmap of z-scores from rlog normalized counts for significantly changing genes across treatment and timepoints (days of treatment).

SASP and cell cycle genes annotated in dark green and blue, respectively. Number assigned to each cluster is shown on the right side under RNA cluster.

D. Heatmap of z-scores from VST-normalized read counts under ATAC-seq peaks with significantly increased accessibility over time (relative to Cycling or day 3). Peaks are categorized as: (1) Palbo-upregulated, (2) Shared-up (upregulated in both drugs), or (3) Doxo-upregulated. Annotations indicate significance in Palbo (pink) or Doxo (green) and their genomic location (Peak annotation: distal, gene body, or promoter).

E. Heatmap of z-scores from VST-normalized read counts under ATAC-seq peaks with significantly decreasing accessibility over time (relative to Cycling or day 3). Peaks are categorized as: (1) Palbo-downregulated, (2) Shared-down (downregulated in both drugs), or (3) Doxo-downregulated. Counts matrix and annotation of peaks were generated the same way as in Figure 2D.

Figure 3: p53 activity in senescence is dependent on DNA damage

A. GSEA running enrichment score for the Hallmark term “P53 PATHWAY” in day 14 Doxo vs. Cycling and day 14 Palbo vs. Cycling comparisons. “P53 PATHWAY” is significantly enriched in day 14 Doxo but not day 14 Palbo.

B. Log2 fold change (log2FC) values of significantly changing genes under enriched Hallmark term, “P53 PATHWAY.”

C. Normalized RNA-seq counts of *CDKN1A* (p21) & *MDM2*, well-known p53 targets, over time.

D. Venn diagram showing the number of p53 target genes that overlap with SASP and NF-κB target genes relative to all Doxo-upregulated genes (RNA cluster 5 & 6 from Figure 2C).

E. Venn diagram showing the number of p53 target genes that overlap with SASP and NF-κB target genes relative to all Palbo-upregulated genes (RNA cluster 3 & 4 from Figure 2C).

F. Log2 fold change (log2FC) values across all significantly changing p53 target genes in day 14 Palbo and day 14 Doxo, relative to Cycling. Paired student t-test shows difference between Palbo and Doxo is significant, with *P*-value = 4.47×10^{-8}.

G. Tn5 insertion sites around aggregated p53 motifs overlapping Doxo- (left), Shared- (middle), or Palbo-upregulated (right) ATAC-seq peaks relative to Cycling (peaks from Figure 2D). The number of overlapping peaks with p53 motifs per condition is shown.

Figure 4: Differential regulatory pathways distinguish doxorubicin and palbociclib driven therapy-induced senescence

A. Log2 fold change (log2FC) values of differentially upregulated genes from RNA-seq clusters in Figure 2C, across different timepoints (days of treatment) and drug conditions, relative to Cycling or day 3 controls within each drug treatment.
B. Activation scores of the most differentially activated predicted upstream regulators between Doxo and Palbo samples, corresponding to RNA clusters in Figure 4A. Differentially activated regulators were identified by summing activation scores across timepoints within each treatment and ranking them from highest to lowest (see STAR Methods). A black outline marks the timepoint used to generate networks from IPA core analysis. Predicted relationships are shown (right) for each RNA cluster with legend at the bottom-right indicating the confidence and type of predicted relationships.
C. MEME-AME analysis of the top 7 differentially enriched motifs in upregulated ATAC-seq peaks at each timepoint, relative to Cycling or day 3 controls within each treatment. First, peaks increasing in accessibility were identified at each timepoint. Then, for each timepoint, Palbo-upregulated peaks were directly compared to Doxo-upregulated peaks (MEME-AME) to identify motifs more enriched in one condition relative to the other. Left: Motifs more enriched in Palbo-upregulated ATAC-seq peaks (foreground) compared to Doxo-upregulated peaks (background). Right: Motifs more enriched in Doxo-upregulated ATAC-seq peaks (foreground) compared to Palbo-upregulated peaks (background). Dot intensity represents -log10(*Padj*) values, while dot size reflects the difference between true positive and false positive peaks (%TP - %FP).

Figure 5: A shared senescence transcriptomic signature driven by NF-κB signaling is delayed in CDK4/6i treatment across cancer cell types

A. -Log10(Padj) values of GO enrichment results for Shared-upregulated genes relative to other RNA-seq clusters in LS8817 cells.
B. -Log10(Padj) values of top 5 IPA predicted upstream regulator complexes and transcriptional regulators of Shared-upregulated genes relative to other RNA-seq clusters in LS8817 cells.
C. GSEA running enrichment score for enriched Hallmark term “TNFA SIGNALING VIA NFKB.” Left: day 14 Doxo and day 14 Palbo vs. Cycling. Right: day 14 Doxo and day 14 Palbo vs. day 3 within each drug treatment in LS8817 cells. Padj values from GSEA are shown.
D. Number of NF-κB target genes overlapping with p53 and SASP target genes relative to all Shared-upregulated genes in LS8817 cells.
E. Log2 fold change (log2FC) values of NF-κB target genes that are part of the Shared-upregulated genes (RNA Cluster 7) in day 3 and day 14 Palbo and Doxo relative to Cycling in LS8817 cells. Median log2FC values for each condition are shown as a bold white line. The dotted gray line at log2FC = 0 indicates no

change from Cycling. A paired Student's t-test was used to assess significance between log2FC distributions.

F. Representative images of SABgal staining (top) and quantification of percentage of SABgal+ MCF7 cells over time (bottom). The scale bar is 50 µm.

G. Representative images showing different levels of DNA damage (γH2AX foci & 53BP1 foci) in doxorubicin and palbociclib treated MCF7's over time. Cells were treated with 100nM doxorubicin or 100nM palbociclib + 10nM fulvestrant. The scale bar is 10 µm.

H. K-means clustered heatmap of z-scores from rlog normalized counts for significantly changing genes across treatment and timepoints (days of treatment) based on RNA-seq performed in MCF-7 cells. SASP and cell cycle genes are annotated in dark green and blue, respectively. NF-kB target genes found in each upregulated gene cluster are shown left of the heatmap. Genes in dark green are also annotated as SASP. GO enrichment results of NF-kB related terms from each RNA-seq cluster in MCF7's.

Figure 6: Increased chromatin accessibility at putative NF-κB binding sites occurs in both types of therapy-induced senescence

A. Left: Schematic illustrating the selection of upregulated ATAC-seq peak sets for MEME-AME motif enrichment analysis. Right: -Log10(*Padj*) values from MEME-AME of NF-κB family of motifs in upregulated ATAC-seq peaks relative to downregulated peaks (based on differential accessibility relative to Cycling) within each drug. The timepoints indicated represent the peak sets chosen as input for MEME-AME. Dot intensity represents -log10(*Padj*) values, while dot size reflects the difference between true positive and false positive peaks (%TP - %FP).

B. Venn diagram showing the number of upregulated ATAC-seq peaks in each drug category from Figure 2D that contain NF-κB family of motifs relative to all upregulated peaks.

C. Tn5 insertion site profiles around aggregated NFKB1 motifs near shared upregulated genes (RNA Cluster 7). ATAC-seq peaks were filtered to include only those with increased accessibility at any timepoint in Doxo or Palbo samples compared to Cycling or day 3 controls within each drug. The number of overlapping peaks with NFKB1 motifs near Shared-upregulated genes per condition is shown.

D. Genome browser visualization of ATAC-seq signal around shared upregulated SASP and NF-κB target genes, *IL1A* & *IL1B* (top) and *CXCL1* & *CXCL8* (bottom). Regions of increased accessibility are highlighted in shaded boxes. Putative RelA (p65) binding sites are shown based on the ReMap database. Putative regulatory enhancers linked to *IL1A*, *IL1B*, *CXCL1*, and *CXCL8* are represented as arc plots

using geneHancer data. CUT&Tag signal for H3K27ac (gold) and H3K27me3 (olive green) in LS8817 untreated cycling cells is also displayed.

Figure 7: Distinct components of the SASP, including NF-κB, can be uncoupled from stable cell cycle arrest

A. Left: Representative images of nuclear localization of p65 subunit of NF-κB over time at 60x magnification. The scale bar is 15 µm. Right: Quantification of log10 ratio of mean intensity of p65 in the nucleus to perinuclear region. Statistical significance was calculated using Dunnett's test.
B. Schematic of pharmacological inhibition of NF-κB with BAY11-7082 (BAY) (see STAR Methods). 10 µM BAY or equivalent volume of DMSO (negative control) was added to cells for 2-3 days prior to harvest.
C. RT-qPCR results of palbociclib or doxorubicin treated cells with or without BAY. Relative fold change values to Cycling are shown. Dotted grey line indicates no change. Diamonds inside boxplot represent the mean fold change value. Circles, triangles, and rectangles represent the fold change of individual biological replicate. Dark purple and dark green shades indicate Palbo and Doxo samples treated with BAY, while lighter purple and green shades indicate samples that had DMSO added at the same time as BAY samples. Statistical significance was calculated using a two-tailed t-test.
D. Crystal violet staining after clonogenic outgrowth after palbociclib or doxorubicin treatment +/- BAY. 800 cells were seeded per well in a 6-well plate in drug-free media for 12 days after harvest.
E. RT-qPCR results of palbociclib treated cells with or without TEAD inhibitor, MYF-01-37 (MYF). Relative fold change values to Cycling are shown. Dotted grey line indicates no change. Diamonds inside boxplot represent the mean fold change value. Circles, triangles, and rectangles represent the fold change of individual biological replicate. Statistical significance was calculated using a two-tailed t-test.
F. Crystal violet staining after clonogenic outgrowth after palbociclib treatment +/- MYF. 800 cells were seeded per well in a 6-well plate and grown in drug-free media for 12 days after harvest.

Figure 8: Summary model showing differences in how CDK4/6i and doxorubicin may activate NF-κB and subsequently the shared SASP

A. NF-κB activation leads to the shared senescence response across treatments. The shared SASP driven by NF-κB can be suppressed with BAY11-7082. A component of the SASP more strongly upregulated in CDK4/6i can also be suppressed by inhibiting TEAD activity. Differences across drugs in enriched transcription factor (TF) motifs at upregulated ATAC-seq peaks, such as AP-1,

CEBPB, GATA3, MEF2A and TEAD4 may contribute to differences in NF-κB regulation. DSB=double-stranded break.

B. Z-scores from rlog normalized counts of induced SASP genes common across treatments and cancer cell types. SASP genes in red are also annotated as NF-κB target genes.

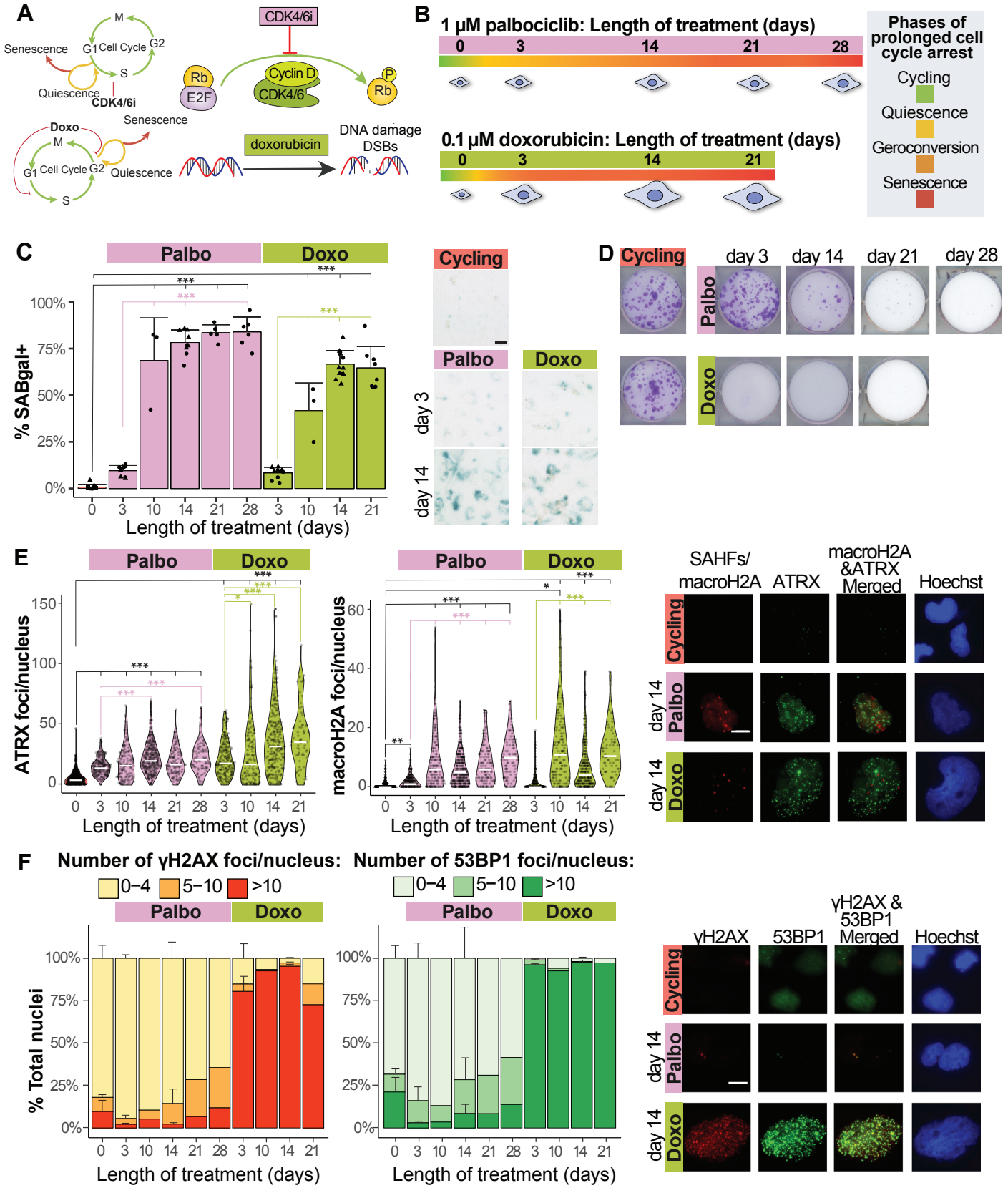

Figure 1: CDK4/6i and doxorubicin both induce senescence features with distinct DNA damage levels

A. Diagram summarizing CDK4/6i (Palbo) vs. doxorubicin (Doxo) mechanisms of cell cycle arrest.

B. Experimental design of drug comparison time course.

C. Left: Percent nuclei counted that had cellular SABgal+ staining at different timepoints. Number of nuclei counted was > 300 per condition at 10x magnification. Each point represents a field of view, with different shapes indicating biological replicates. Error bars denote standard deviation. Statistical significance was calculated using Dunnett's test. Right: Representative SABgal staining images at day 3 and day 14 shown at 10x magnification with scale bar = 50 μm.

D. Crystal violet staining after clonogenic outgrowth for 10-12 days. 800 cells were seeded per well in a 6-well plate in drug-free media after completion of drug treatment at each timepoint.

E. Number of ATRX foci (left) and macroH2A foci (indicative of SAHFs; middle) per nucleus was counted for ~100 nuclei per timepoint. Representative images are shown at day 14 of each drug treatment at 60x magnification (right). Significance was calculated using Dunnett's test. The scale bar is 15 μm.

F. Number of γH2AX foci (indicative of DNA damage; left) & 53BP1 foci (indicative of DNA repair; middle) per nucleus was counted for ~100 nuclei per timepoint & categorized in 0-4, 5-10 or >10 foci/nuclei. Representative images are shown at day 14 of each drug treatment at 60x magnification (right). The scale bar is 15 μm.

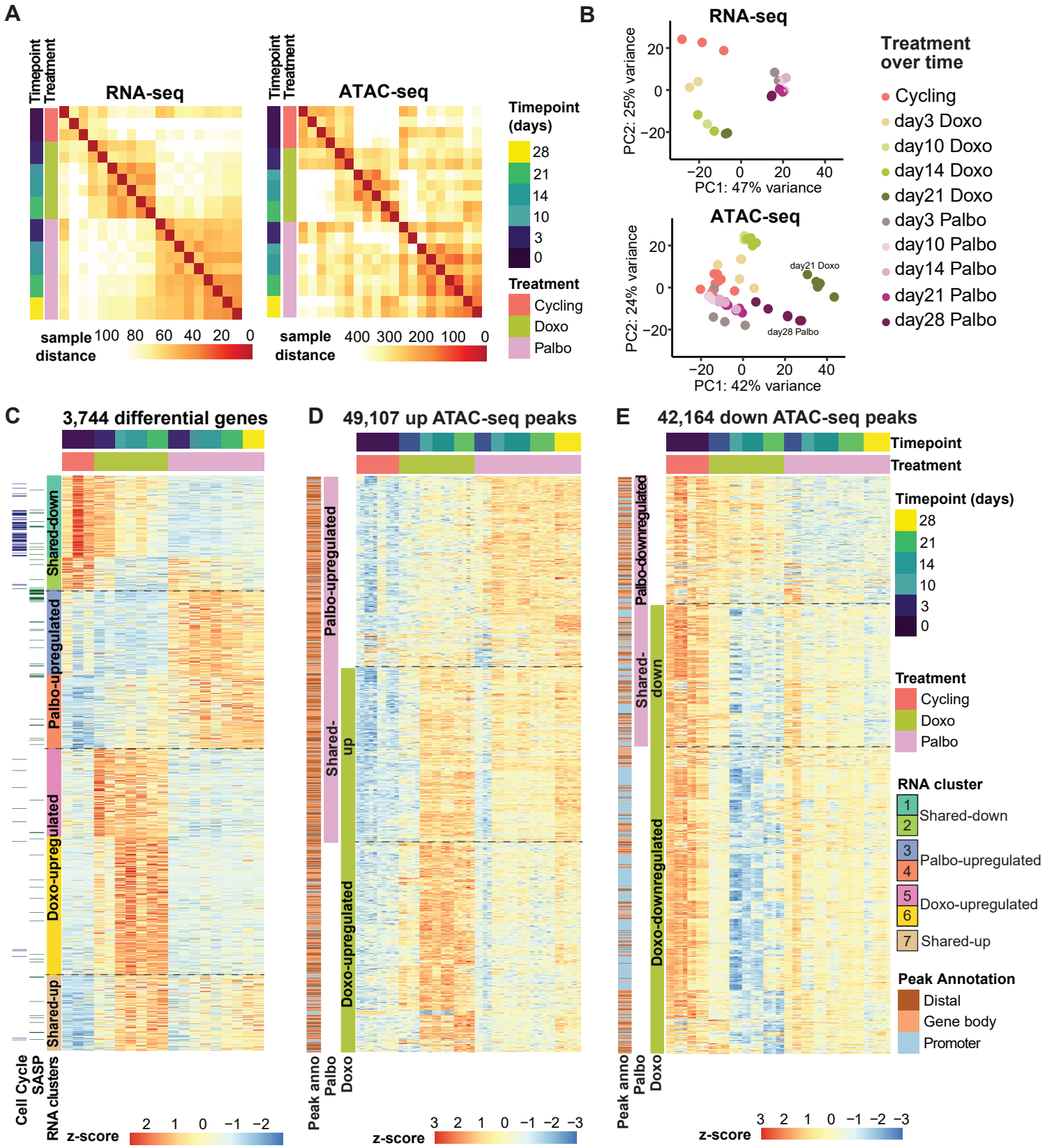

Figure 2: Distinct and shared transcriptional and chromatin responses define drug-specific senescence trajectories

A. Distance measures between samples ordered by treatment and timepoint.
B. Principal component analysis on RNA-seq and ATAC-seq samples.
C. K-means clustered heatmap of z-scores from rlog normalized counts for significantly changing genes across treatment and timepoints (days of treatment). SASP and cell cycle genes annotated in dark green and blue, respectively. Number assigned to RNA cluster is shown on the right.
D. Heatmap of z-scores from VST-normalized read counts under ATAC-seq peaks with significantly increased accessibility over time (relative to Cycling or day 3). Peaks are categorized as: (1) Palbo-upregulated, (2) Shared-up (upregulated in both drugs), or (3) Doxo-upregulated. Annotations indicate significance in Palbo (pink) or Doxo (green) and their genomic location (Peak annotation: distal, gene body, or promoter).
E. Heatmap of z-scores from VST-normalized read counts under ATAC-seq peaks with significantly decreasing accessibility over time (relative to Cycling or day 3). Peaks are categorized as: (1) Palbo-downregulated, (2) Shared-down (downregulated in both drugs), or (3) Doxo-downregulated. Counts matrix and annotation of peaks were generated the same way as upregulated ATAC-seq peaks in Figure 2D.

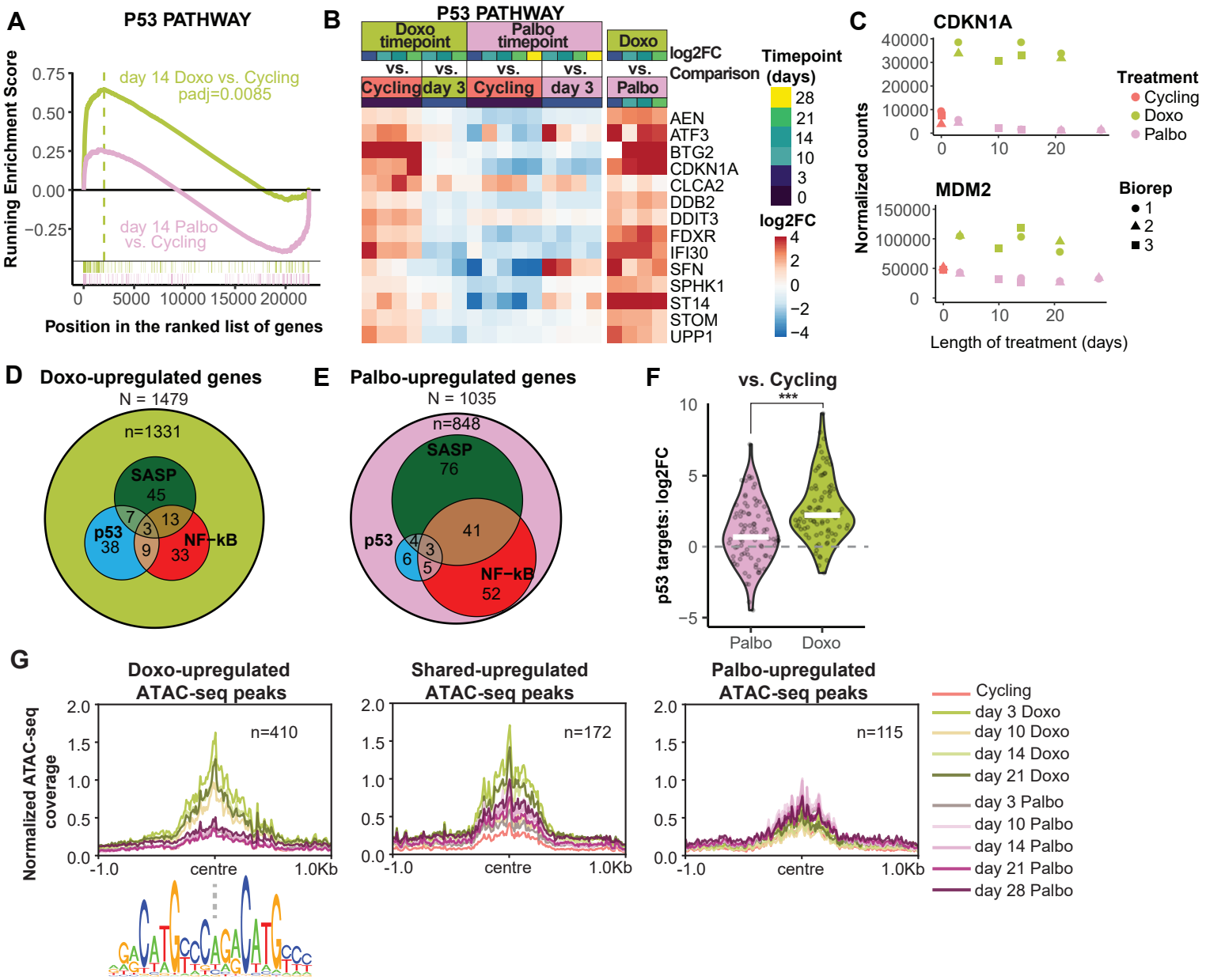

Figure 3: p53 activity in senescence is dependent on DNA damage

A. GSEA running enrichment score for the Hallmark term "P53 PATHWAY" in day 14 Doxo vs. Cycling and day 14 Palbo vs. Cycling comparison. "P53 PATHWAY" is significantly enriched in day 14 Doxo but not day 14 Palbo.
B. Log2 fold change (log2FC) values of significantly changing genes under enriched Hallmark term, "P53 PATHWAY."
C. Normalized RNA-seq counts of *CDKN1A* (p21) & *MDM2*, well-known p53 targets, over time.
D. Venn diagram showing the number of p53 target genes that overlap with SASP and NF-κB target genes relative to all Doxo-upregulated genes (RNA cluster 5 & 6 from Figure 2C).
E. Venn diagram showing the number of p53 target genes that overlap with SASP and NF-κB target genes relative to all Palbo-upregulated genes (RNA cluster 3 & 4 from Figure 2C).
F. Log2 fold change (log2FC) values across all significantly changing p53 target genes in day 14 Palbo and day 14 Doxo, relative to Cycling. Paired student t-test shows difference between Palbo and Doxo is significant, with *P*-value = 4.468×10^{-8}.
G. Tn5 insertion sites around aggregated p53 motifs overlapping Doxo- (left), Shared- (middle) or Palbo-upregulated (right) ATAC-seq peaks relative to Cycling (peaks from Figure 2D). The number of overlapping peaks with p53 motifs per condition is shown.

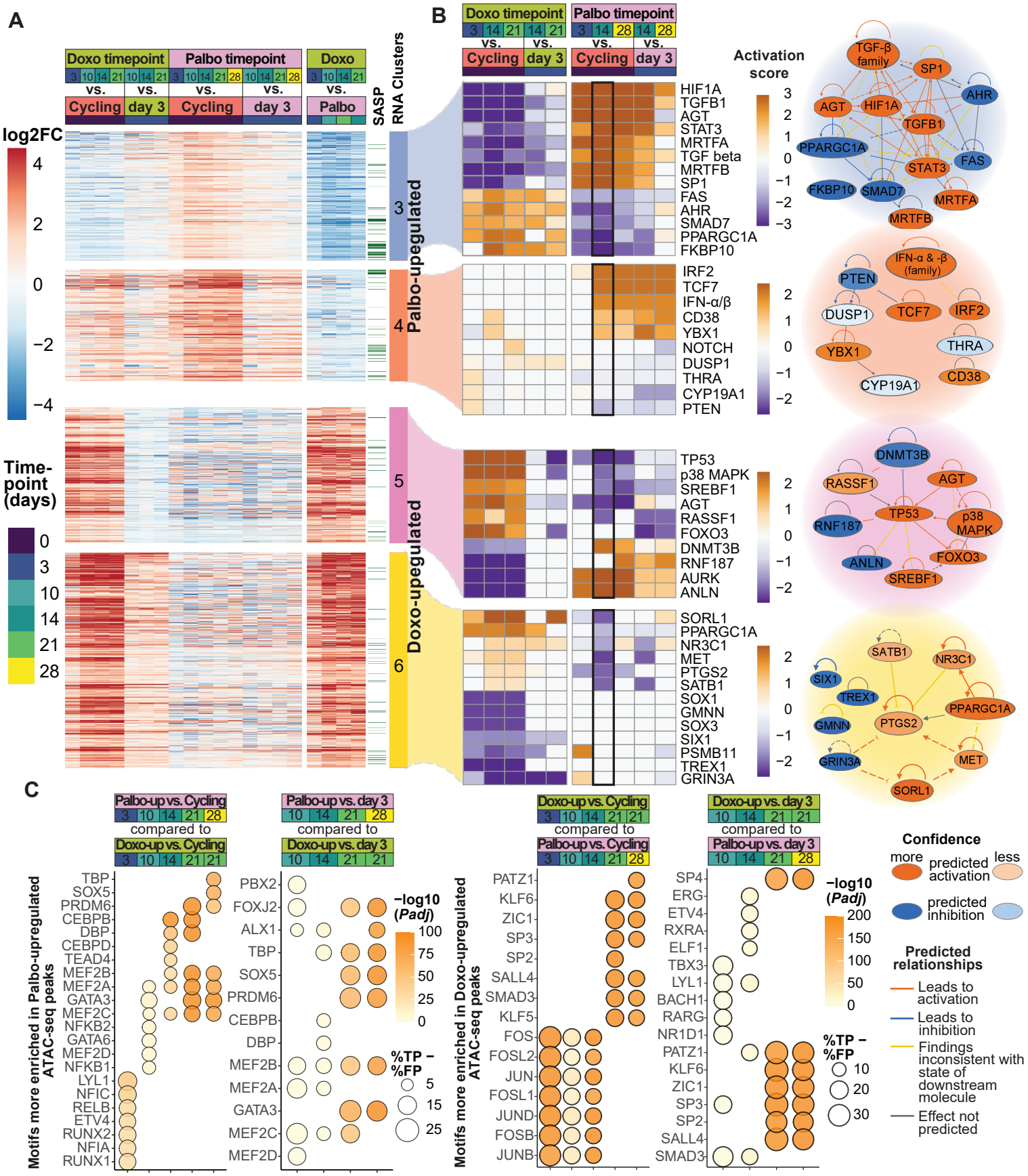

Figure 4: Differential regulatory pathways distinguish doxorubicin- and palbociclib-driven therapy-induced senescence

A. Log2 fold change (log2FC) values of differentially upregulated genes from RNA-seq clusters in Figure 2C, across different timepoints (days of treatment) and drug conditions, relative to Cycling or day 3 controls for each drug treatment.

B. Activation scores of the most differentially activated upstream regulators between Doxo and Palbo, corresponding to RNA clusters in Figure 4A. Differentially activated regulators were identified by summing activation scores across timepoints within each treatment and ranking them from highest to lowest (see Methods). A black outline marks the timepoint used to generate networks from IPA core analysis. Predicted relationships are shown (right) for each RNA cluster with legend at the bottom-right indicating the confidence and type of predicted relationships.

C. MEME-AME analysis of the top 7 differentially enriched motifs in upregulated ATAC-seq peaks at each timepoint, relative to Cycling or day 3 controls within each treatment. First, peaks increasing in accessibility were identified at each timepoint. Then, for each timepoint, Palbo-upregulated peaks were directly compared to Doxo-upregulated peaks (MEME-AME) to identify motifs more enriched in one condition relative to the other. Left: Motifs more enriched in Palbo-upregulated ATAC-seq peaks (foreground) compared to Doxo-upregulated peaks (background). Right: Motifs more enriched in Doxo-upregulated ATAC-seq peaks (foreground) compared to Palbo-upregulated peaks (background). Dot intensity represents -log10(*Padj*) values, while dot size reflects the difference between true positive and false positive peaks (%TP - %FP).

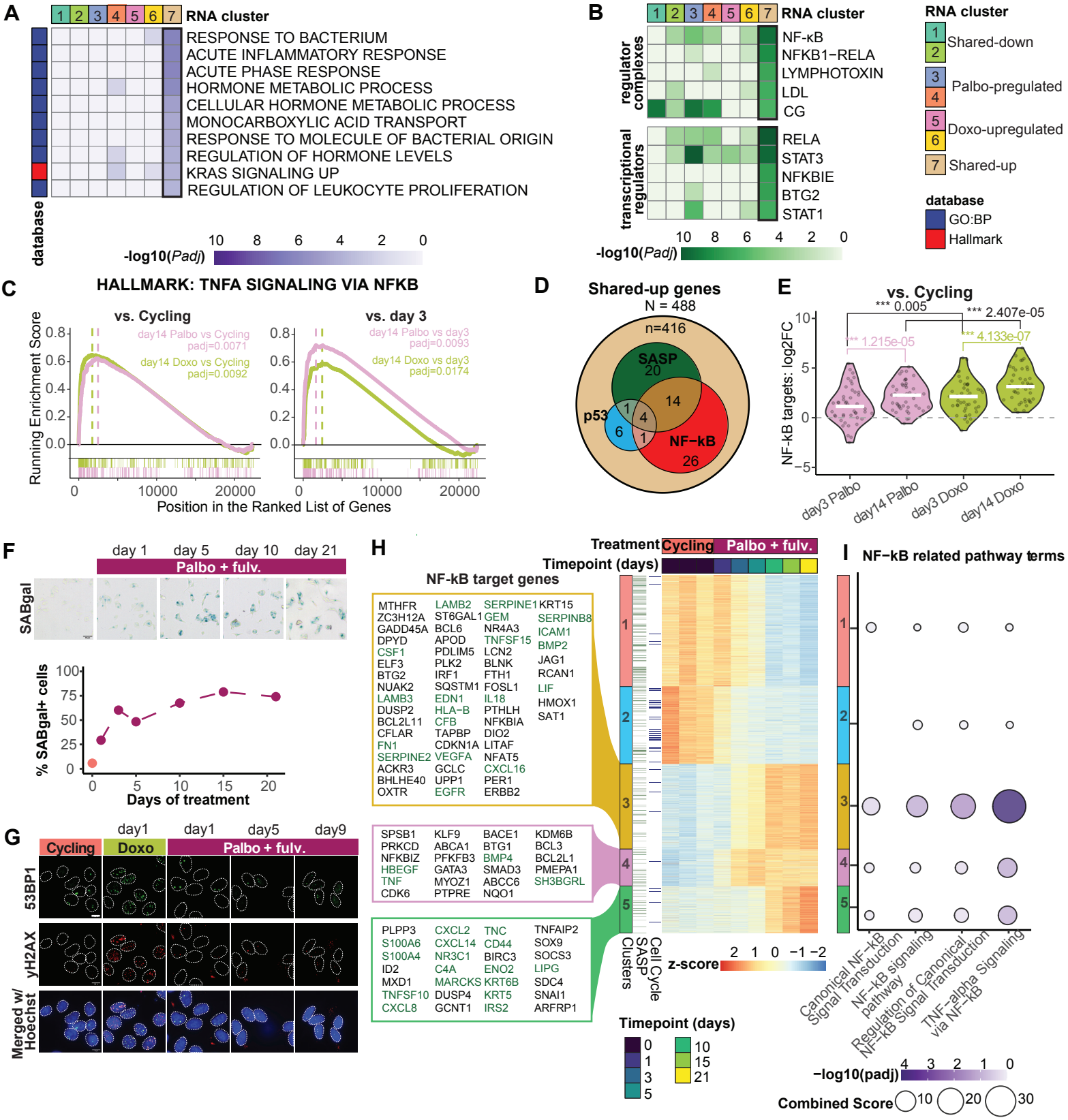

Figure 5: A shared senescence transcriptomic signature driven by NF-κB signaling is delayed in CDK4/6i treatment across cancer cell types

A. -Log10(*Padj*) values of GO enrichment results for Shared-upregulated genes relative to other RNA-seq clusters in LS8817 cells.
B. -Log10(*Padj*) values of top 5 IPA predicted upstream regulator complexes and transcriptional regulators of Shared-upregulated genes relative to other RNA-seq clusters in LS8817 cells.
C. GSEA running enrichment score for enriched Hallmark term "TNFA SIGNALING VIA NFKB." Left: day 14 Doxo and day 14 Palbo vs. Cycling. Right: day 14 Doxo and day 14 Palbo vs. day 3 within each drug treatment in LS8817 cells. *Padj* values from GSEA are shown.
D. Number of NF-κB target genes overlapping with p53 and SASP target genes relative to all Shared-upregulated genes in LS8817 cells.
E. Log2 fold change (log2FC) values of NF-κB target genes that are part of the Shared-upregulated genes (RNA Cluster 7) in day 3 and day 14 Palbo and Doxo relative to Cycling in LS8817 cells. Median log2FC values for each condition are shown as a bold white line. The dotted gray line at log2FC = 0 indicates no change from Cycling. A paired Student's t-test was used to assess significance between log2FC distributions.
F. Representative images of SABgal staining (top) and quantification of percentage of SABgal+ MCF7 cells over time (bottom). The scale bar is 50 μm.
G. Representative images showing different levels of DNA damage (γH2AX foci & 53BP1 foci) in doxorubicin and palbociclib treated MCF7's over time. Cells were treated with 100nM doxorubicin or 100nM palbociclib + 10nM fulvestrant. The scale bar is 10 μm.
H. K-means clustered heatmap of z-scores from rlog normalized counts for significantly changing genes across treatment and timepoints (days of treatment) based on RNA-seq performed in MCF-7 cells. SASP and cell cycle genes are annotated in dark green and blue, respectively. NF-kB target genes found in each upregulated gene cluster are shown left of the heatmap. Genes in dark green are also annotated as SASP.
I. GO enrichment results of NF-kB related terms from each RNA-seq cluster in MCF7's.

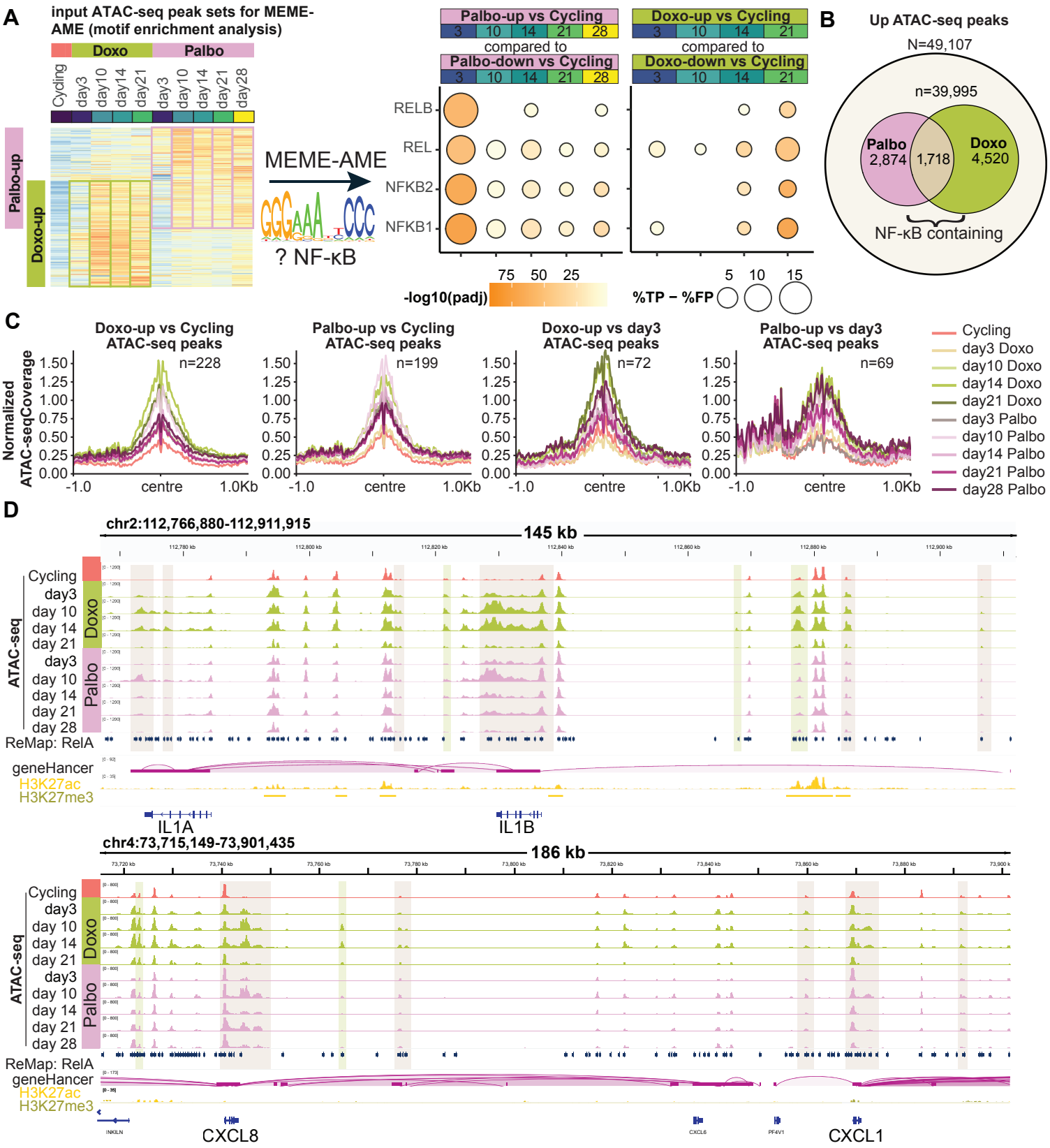

Figure 6: Increased chromatin accessibility at putative NF-kB binding sites occur in both types of therapy induced senescence

A. Left: Schematic illustrating the selection of upregulated ATAC-seq peak sets for MEME-AME motif enrichment analysis. Right: -Log10(Padj) values from MEME-AME of NF-κB family of motifs in up-regulated ATAC-seq peaks relative to down-regulated peaks (based on differential accessibility relative to Cycling) within each drug. The timepoints indicated represent the peak sets chosen as input for MEME-AME. Dot intensity represents -log10(p-adj) values, while dot size reflects the difference between true positive and false positive peaks (%TP - %FP).

B. Venn diagram showing the number of upregulated ATAC-seq peaks in each drug category from Fig 2D that contain NF-κB family of motifs relative to all upregulated peaks.

C. Tn5 insertion site profiles around aggregated NFKB1 motifs near shared upregulated genes (RNA Cluster 7). ATAC-seq peaks were filtered to include only those with increased accessibility at any timepoint in response to Doxo or Palbo compared to Cycling or day 3 controls within each drug. The number of overlapping peaks with NFKB1 motifs near Shared-upregulated genes per condition is shown.

D. Genome browser visualization of ATAC-seq signal around shared upregulated SASP and NF-κB target genes, IL1A & IL1B (top) and CXCL1 & CXCL8 (bottom). Regions of increased accessibility are highlighted in shaded boxes. Putative RelA (p65) binding sites are shown based on the ReMap database. Putative regulatory enhancers linked to IL1A and IL1B are represented as arc plots using geneHancer data. CUT&Tag signal for H3K27ac (gold) and H3K27me3 (olive green) in LS8817 untreated cycling cells is also displayed.

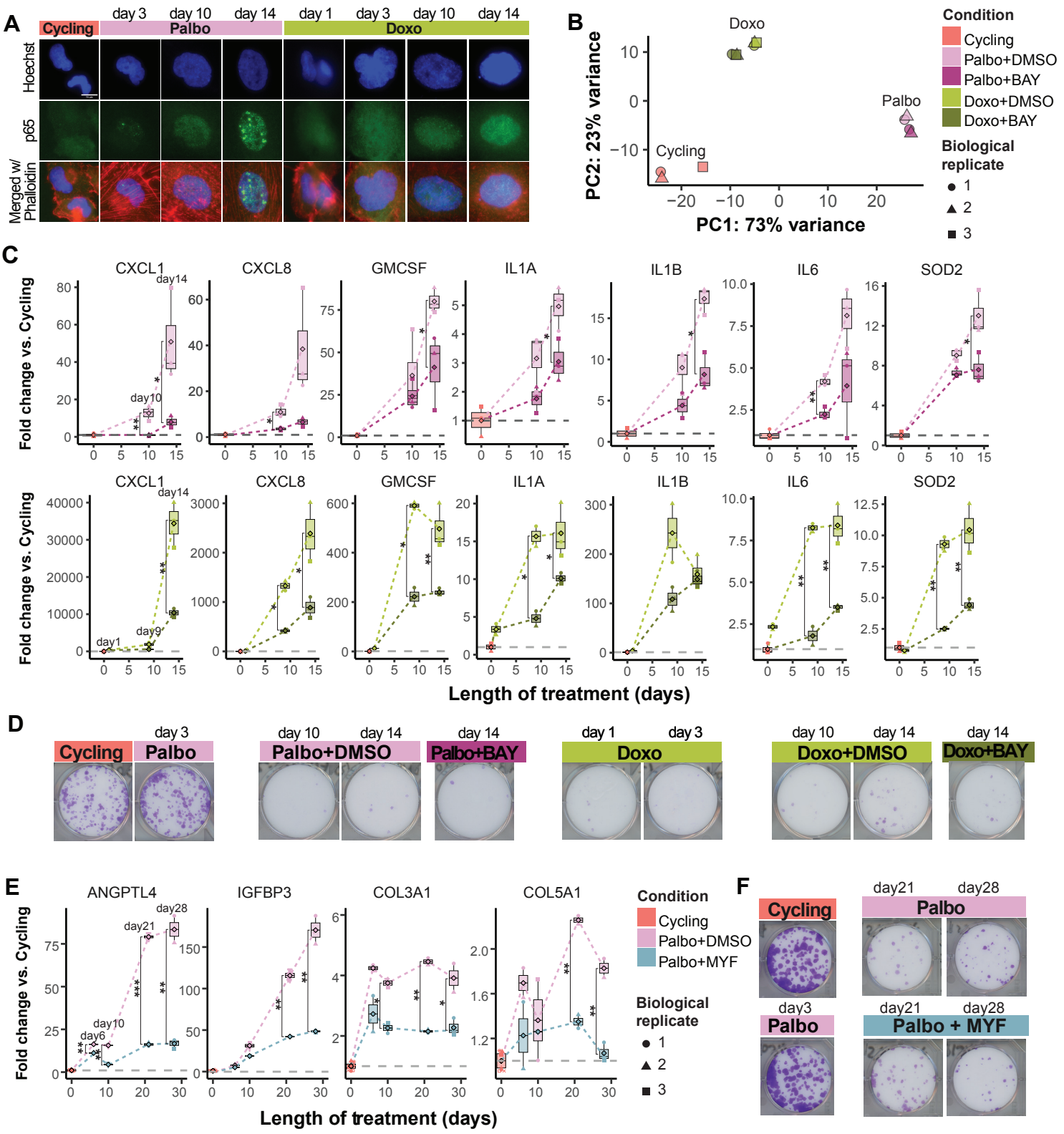

Figure 7: Distinct components of the SASP, including NF-κB, can be uncoupled from stable cell cycle arrest

A. Representative images of nuclear localization of p65 subunit of NF-κB over time at 60x magnification. The scale bar is 15 μm.
B. Principal component analysis on RNA-seq of day14 palbociclib or doxorubicin treated cells with or without NF-κB inhibitor, BAY11-7082 (BAY).
C. RT-qPCR results of palbociclib or doxorubicin treated cells with or without BAY. Relative fold change values to Cycling are shown. Dotted grey line indicates no change. Diamonds inside boxplot represent the mean fold change value. Circles, triangles, and rectangles represent the fold change of individual biological replicate. Dark purple and dark green shades indicate Palbo and Doxo samples treated with BAY while lighter purple and green shades indicate samples that had DMSO added at the same time as BAY samples. Statistical significance was calculated using a two-tailed t-test.
D. Crystal violet staining after clonogenic outgrowth after palbociclib or doxorubicin treatment +/- BAY. 800 cells were seeded per well in a 6-well plate and grown in drug-free media for 12 days after harvest.
E. RT-qPCR results of palbociclib treated cells with or without TEAD inhibitor, MYF-01-37 (MYF). Relative fold change values to Cycling are shown. Dotted grey line indicates no change. Diamonds inside boxplot represent the mean fold change value. Circles, triangles, and rectangles represent the fold change of individual biological replicate. Statistical significance was calculated using a two-tailed t-test.
F. Crystal violet staining after clonogenic outgrowth after palbociclib treatment +/- MYF. 800 cells were seeded per well in a 6-well plate and grown in drug-free media for 12 days after harvest.

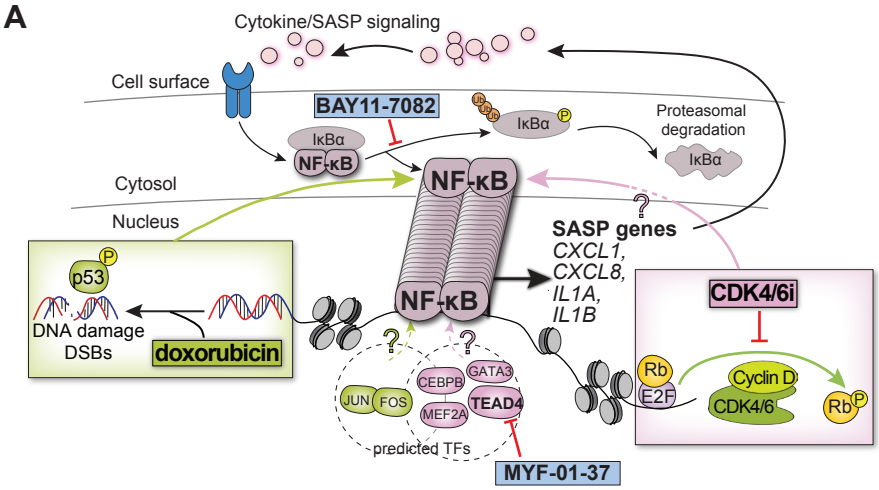

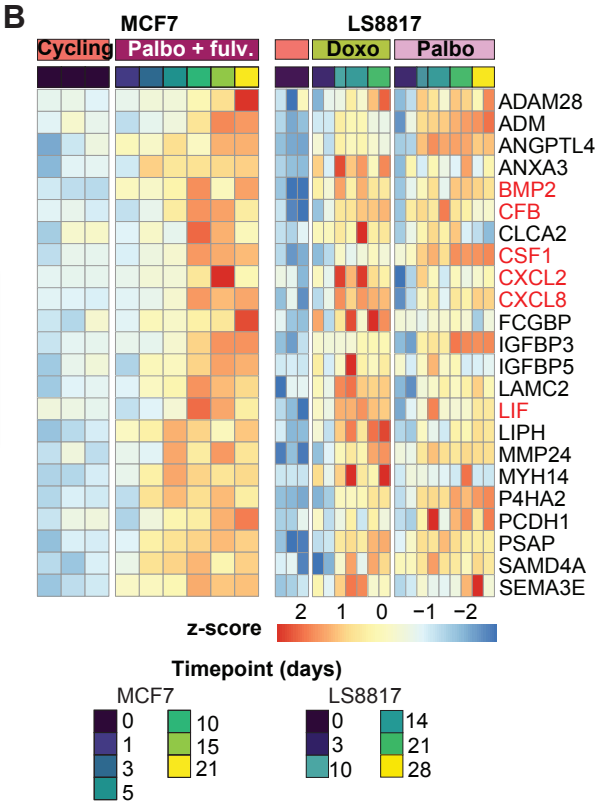

Figure 8: Summary model showing differences in how CDK4/6i and doxorubicin may activate NF-κB and subsequently the shared SASP.

A. NF-κB activation leads to the shared senescence response across treatments. The shared SASP driven by NF-κB can be suppressed with BAY11-7082. A component of the SASP more strongly upregulated in CDK4/6i can also be suppressed by inhibiting TEAD activity. Differences across drugs in enriched transcription factor (TF) motifs at upregulated ATAC-seq peaks, such as AP-1, CEBPB, GATA3, MEF2A and TEAD4 may contribute to differences in NF-κB regulation. DSB=double-stranded break.

B. Z-scores from rlog normalized counts of induced SASP genes common across treatments and cancer cell types. SASP genes in red are also annotated as NF-κB target genes.